

Growth of Jupiter: Enhancement of core accretion by a voluminous low-mass envelope

Gennaro D'Angelo^{a,b,*,1}, Stuart J. Weidenschilling^c, Jack J. Lissauer^a, Peter Bodenheimer^d

^a NASA Ames Research Center, Space Science and Astrobiology Division, MS 245-3, Moffett Field, CA 94035, USA

^b SETI Institute, 189 Bernardo Ave., Mountain View, CA 94043, USA

^c Planetary Science Institute, 1700 East Fort Lowell Road, Suite 106, Tucson, AZ 85719-2395, USA

^d UCO/Lick Observatory, Department of Astronomy and Astrophysics, University of California, Santa Cruz, CA 95064, USA

ARTICLE INFO

Article history:

Received 26 August 2013

Revised 27 June 2014

Accepted 27 June 2014

Available online 10 July 2014

Keywords:

Accretion

Jovian planets

Jupiter

Planetary formation

Planetesimals

Article in press. This is an unofficial preprint prepared by the authors from the accepted manuscript.

ABSTRACT

We present calculations of the early stages of the formation of Jupiter via core nucleated accretion and gas capture. The core begins as a seed body of about 350 kilometers in radius and orbits in a swarm of planetesimals whose initial radii range from 15 meters to 50 kilometers. The evolution of the swarm accounts for growth and fragmentation, viscous and gravitational stirring, and for drag-assisted migration and velocity damping. During this evolution, less than 9% of the mass is in planetesimals smaller than 1 kilometer in radius; $\lesssim 25\%$ is in planetesimals with radii between 1 and 10 kilometers; and $\lesssim 7\%$ is in bodies with radii larger than 100 kilometers. Gas capture by the core substantially enhances the size-dependent cross-section of the planet for accretion of planetesimals. The calculation of dust opacity in the planet's envelope accounts for coagulation and sedimentation of dust particles released as planetesimals are ablated. The calculation is carried out at an orbital semi-major axis of 5.2 AU and the initial solids' surface density is 10 g cm^{-2} at that distance. The results give a core mass of nearly 7.3 Earth masses (M_{\oplus}) and an envelope mass of $\approx 0.15 M_{\oplus}$ after about 4×10^5 years, at which point the envelope growth rate surpasses that of the core. The same calculation without the envelope yields a core of only about $4.4 M_{\oplus}$.

© 2014 Published by Elsevier Inc.

1. Introduction

The formation of Jupiter is a key element in the classical problem of the origin of the Solar System. Detailed studies of the formation of this planet by core-nucleated accretion have been carried out for decades (Safronov 1972; Perri and Cameron 1974; Mizuno 1980; Bodenheimer and Pollack 1986; Pollack et al. 1996). The latter work studied what is now considered to be a standard case: the formation of Jupiter, in a fixed orbit at 5.2 AU, in a disk with solid surface density $\sigma_Z = 10 \text{ g cm}^{-2}$, about three times as high as that in the minimum-mass solar nebula (Weidenschilling 1977; Hayashi 1981). Pollack et al.'s basic conclusion was that the formation time can range from 1.25 to 8 Myr, de-

pending on physical assumptions made in the computations. The heavy-element core masses fell in the range 12–20 Earth masses (M_{\oplus}).

Jupiter's growth involves numerous elements of physics over a wide range of mass and length scales. The initial steps in the process involve the buildup of planetesimals from an initial distribution of sub-micron-size dust grains (e.g., Chiang and Youdin 2010). The work described in the present paper starts at a somewhat later stage, when a swarm of planetesimals, with radii ranging from several meters to tens of kilometers, has formed, along with a nascent planetary embryo of somewhat larger size. The embryo (composed almost entirely of elements heavier than hydrogen and helium) builds up by accretion of planetesimals and becomes the planetary core. When its mass reaches $\sim 0.1 M_{\oplus}$, and when the escape speed from its surface exceeds the thermal speed of molecules in the surrounding gas disk, it begins to capture a small amount of gas. This gas is assumed to have nearly solar composition. However, the accretion rate of

* Corresponding author at: NASA Ames Research Center, Space Science and Astrobiology Division, MS 245-3, Moffett Field, CA 94035, USA. Fax: +1-650-604-6779.

E-mail address: gennaro.dangelo@nasa.gov (G. D'Angelo).

¹ Address: Los Alamos National Laboratory, Los Alamos, NM 87545, USA.

solids onto the core (\dot{M}_c) greatly exceeds, for some time, the accretion rate of gas (\dot{M}_e , composed primarily of molecular hydrogen and helium). Once the core has accreted most of the planetesimals within its gravitational reach, \dot{M}_c slows down significantly and \dot{M}_e , which is increasing, begins to exceed it. Thereafter, during a phase characterized by slow gas accretion, M_c continues to grow, but less rapidly than \dot{M}_e , until the *crossover mass* is reached ($M_c = M_e$). We denote by “Phase 1” the time up to the point where $\dot{M}_e = \dot{M}_c$, and by “Phase 2” the time from there up to crossover. At or before crossover, the rapid gas accretion phase begins ($\dot{M}_e \gg \dot{M}_c$). The gas accretion rate is at first limited by the rate at which the envelope can contract and release energy, governed primarily by the opacity due to dust and gas. The contraction rate increases and soon reaches the point where the accretion rate required by the contraction exceeds the rate at which the disk can provide gas. The *disk-limited* accretion phase begins, with the gas accretion rate depending on several factors: planet mass, planet orbital radius, disk gaseous density, disk kinematic viscosity, and disk scale height. The total planet mass (M_p) at which the disk-limited phase starts is typically several tens of Earth masses (Lissauer et al. 2009). Disk-limited accretion rates are determined by three-dimensional hydrodynamics simulations of a planet embedded in a disk (Lissauer et al. 2009; Bodenheimer et al. 2013, and references therein). The final mass of the planet is determined by a combination of gap opening, which drastically reduces accretion, and the dissipation of the nebular gas.

In the case of Jupiter, there are several observational constraints that must be satisfied by any formation model. Protoplanetary disk lifetimes have a median value of ~ 3 Myr and a maximum of ~ 10 Myr (Hillenbrand 2008; Roberge and Kamp 2011). The mass ($M_J = 1.898 \times 10^{30}$ g), equatorial radius ($R_J = 7.15 \times 10^9$ cm) and gravitational moments J_2, J_4, J_6 are measured, constraining the mean density and density distribution. The Galileo probe measured the abundances of a number of elements in Jupiter’s outer layers (Young et al. 1996; Owen et al. 1999; Young 2003) and determined that they were in the range of 2–4 times solar. Derived core masses from models of the interior of Jupiter vary considerably depending on the equation of state and assumed composition layering. Militzer et al. (2008) obtain $M_c = 16 \pm 2 M_\oplus$; Nettelmann et al. (2012) find $M_c = 0\text{--}8 M_\oplus$; Saumon and Guillot (2004) find $M_c = 0\text{--}11 M_\oplus$. The Nettelmann three-layer models are consistent with the abundances measured by Galileo in the atmosphere, and have total heavy-element masses in the range $28\text{--}32 M_\oplus$, about six times solar. However, this quantity is not well constrained. Estimates range from 0 to $18 M_\oplus$ for the core mass M_c , and from 15 to $40 M_\oplus$ for the total heavy-element mass M_Z (Fortney and Nettelmann 2010). In this paper, we do not distinguish between the two masses M_c and M_Z .

Several major improvements in the physical basis of the computations have been made since the work of Pollack et al. (1996). Alibert et al. (2005) and Mordasini et al. (2012) include the effects of disk evolution and planetary orbital migration on the formation process. Lissauer et al. (2009) and Bodenheimer et al. (2013) use gas accretion rates for the disk-limited phase based on three-dimensional hydrodynamic simulations of disk flow around an embedded planet. Movshovitz et al. (2010, hereafter MBPL10) calculate the dust opacity in the envelope of the forming planet

self-consistently by including the effects of dust settling and coagulation. The results of MBPL10 show a significant increase in gas accretion rate prior to the disk-limited phase, due to the reduced opacity (and hence faster cooling) in the outer parts of the planet’s envelope. Inaba et al. (2003) include a statistical treatment of the planetesimal accretion rate onto the core, an improvement over the more approximate treatment of this rate by Pollack et al. (1996). The time to form the initial core is crucial in determining the formation time for the entire planet. They include the enhancement in the capture cross-section for planetesimals as a result of the presence of the gaseous envelope, as well as collisional fragmentation of planetesimals and a range of planetesimal sizes. Inaba et al. (2003) came to the basic conclusion that a very high surface density of solid material in the initial disk, $\sigma_Z = 25 \text{ g cm}^{-2}$ at 5.2 AU, was required to build a core of $21 M_\oplus$ within the lifetime of the protoplanetary disk. This core mass is above the values required to initiate rapid gas accretion (which they did not calculate) but their σ_Z implies a disk mass well above typical observed values. The above result was obtained with assumed interstellar grain opacities in the planet’s atmosphere. If these opacities are reduced by a factor 100, they find that with a smaller value of the surface density, $\sigma_Z = 12.5 \text{ g cm}^{-2}$, a core of $7 M_\oplus$ can form at 5.2 AU in 5 Myr, probably sufficient to collect gas.

The results of Inaba et al. (2003) imply that core formation times at 5.2 AU are actually longer than those calculated by, for example, Pollack et al. (1996) with an assumed $\sigma_Z = 10 \text{ g cm}^{-2}$. Inaba et al. also confirm the findings of Pollack et al. that the grain opacity is an important quantity during initial core formation. If the opacity is reduced, the envelope density must increase to maintain hydrostatic and thermal equilibrium during Phase 1, at a given core accretion rate; thus, more gas flows into the envelope and the capture cross-section for planetesimals is enhanced.

In this paper we consider the initial core formation, Phase 1, at 5.2 AU with $\sigma_Z = 10 \text{ g cm}^{-2}$, a reasonable value for an initial solar nebula (Weidenschilling 2005). The main question to be answered is whether or not a core of $5\text{--}10 M_\oplus$ can be formed on a timescale of less than $1\text{--}2$ Myr. An initial core (at the end of Phase 1) in that mass range is likely to accrete gas and build up to a Jupiter mass in less than a typical disk lifetime (MBPL10). To answer that question we combine two state-of-the-art codes, one for the statistical treatment of planetesimal accretion, and the other for the calculation of the structure, evolution, and capture cross-sections of the planet’s gaseous envelope. The grain opacity in the envelope includes the effects of coagulation and settling. The two codes interact, in that the planetesimal code provides \dot{M}_c while the envelope code provides M_e and the capture radius for each planetesimal size in the assumed range. The details of the codes are presented in Section 2. Previous relevant studies and some of their findings are briefly reviewed in Section 3. Our results are discussed in Section 4, and compared with parallel calculations (i) without the presence of the envelope, and (ii) with the envelope but with the core accretion rates used in previous works including Pollack et al. (1996) and MBPL10. The conclusions are presented in Section 5.

2. Numerical procedures

In this section, we outline the main numerical procedures that are employed in our models of Jupiter’s core accumu-

lation and envelope formation.

2.1. The planetesimal accretion code

A detailed discussion of the solid-body accretion code is presented in [Weidenschilling et al. \(1997, see also Weidenschilling, 2011\)](#). Here we present a general summary of the method and the procedure as used in the simulations. The accretion code computes collisional and gravitational interactions within a swarm of planetesimals extending over a wide range of heliocentric distances. The swarm is divided into a number of radial zones, each corresponding to a narrow range of semi-major axes. Within each of these zones, the size-frequency distribution is represented by the number of bodies in each of a series of logarithmic diameter bins, chosen so that the mean mass differs by a factor of two between adjacent bins. Each bin has mean values of orbital eccentricity and inclination, with an assumed range about the mean. During a time-step, all zone/bin combinations that have crossing orbits are identified. Impact probabilities are computed, based on the relative velocities, gravitationally enhanced collisional cross-sections, and the fractional overlap of orbits. Based on these probabilities, the locations of a set of typical collisions are selected stochastically, and the corresponding impact velocities are evaluated. The outcome of an impact depends on the velocity, the mass ratio of projectile and target, and their size-dependent impact strength, which includes gravitational binding energy. Either or both bodies may be eroded or shattered. Fragments are assumed to have a power-law size distribution; for shattering events the slope of this distribution depends on the specific energy. A fraction (1%) of the impact energy in the center of mass frame is partitioned into kinetic energy of the fragments. Depending on the escape velocity of the colliding bodies, some fraction of the mass may escape, or it all may be accreted. The merged body is assumed to have the velocity of the center of mass, while escaping fragments are assigned a mean velocity with a randomly chosen direction relative to that vector. New orbits are computed from these velocity components, and the appropriate amounts of mass are added to the corresponding bins and zones. Thus, collisions can transfer mass between radial zones, in addition to causing the size distribution to evolve with time.

Eccentricities and inclinations evolve separately due to viscous stirring and dynamical friction. The rates for velocity evolution due to interactions among the bodies in the swarm are modeled by the formulae of [Wetherill and Stewart \(1989\)](#). Collisions, modeled as described above, have a net damping effect on velocities. As nebular gas is assumed to be present during Jupiter's formation, gas drag also acts to damp eccentricities and inclinations ([Adachi et al. 1976](#)). As the accretion code assumes Keplerian dynamics for the planetesimals, it is not realistic to track the fates of bodies smaller than ~ 10 meters in size, for which gas drag causes rapid orbital evolution. Such bodies would presumably be lost by spiraling inward toward the Sun on short timescales. In fact, denoting with a , Ω , and R the initial semi-major axis, orbital frequency, and radius of the body, and assuming a drag coefficient of order unity, the timescale τ_{drag} for orbital decay due to gas drag is

$$\Omega\tau_{\text{drag}} \sim \frac{16}{3} \left(\frac{\rho_s}{\rho_{\text{neb}}} \right) \left(\frac{R}{a} \right) \left(\frac{a}{H} \right)^4, \quad (1)$$

where ρ_s and ρ_{neb} indicate the density of the body and the nebular gas, respectively. The ratio H/a is the local aspect

ratio of the nebula (the relative pressure scale height), and quantifies the deviation from Keplerian rotation (Ω_K) of the gas. Typically, Ω is such that $(\Omega_K - \Omega)/\Omega_K \sim (H/a)^2$. For 10 m-size bodies, the conditions used here (see Section 2.2) result in a variation $\gtrsim 10\%$ in semi-major axis over a few tens of orbital periods. We assume that all fragments smaller than 15 m are lost; in our simulations this loss is typically $< 10\%$ of the total mass of the swarm.

The assumption that the majority of these small fragments are lost, and not accreted by the dominant body, or core, can be proven by showing that the time to cross (in the radial direction) the core's libration region of half-width w , $\tau_{\text{cross}} \sim \tau_{\text{drag}}(2w/a)$, is much shorter than the libration timescale of a fragment, $\tau_{\text{lib}} = 8\pi a/(3\Omega w)$. Using Equation (1), the ratio of the two timescales becomes

$$\frac{\tau_{\text{cross}}}{\tau_{\text{lib}}} \sim \left(\frac{\rho_s}{\rho_{\text{neb}}} \right) \left(\frac{R}{a} \right) \left(\frac{a}{H} \right)^4 \left(\frac{w}{a} \right)^2. \quad (2)$$

When w is about equal to the Hill radius, $R_H = a[M_p/(3M_\odot)]^{1/3}$, the ratio in Equation (2) is ~ 0.01 for a 10 m-size fragment and a 5 Earth-mass core, and its value is even less for smaller fragment size and/or core mass. More detailed calculations leading to the same conclusion are presented by [Kary et al. \(1993\)](#); [Kary and Lissauer \(1995\)](#).

The evolution of the planetesimal swarm is dominated by its interactions with the growing Jovian core, which becomes much larger than the remaining bodies. Due to conservation of the Jacobi parameter in the restricted 3-body problem, a small body whose orbit crosses that of a single massive body is stirred less effectively than one that can encounter more than one massive body. In principle, the Jacobi parameter allows close encounters for orbits that are initially separated in semi-major axis by up to $2\sqrt{3}R_H$. However, only a limited range of separations between about 1.8 and $2.4R_H$ allow a planetesimal with an initially circular orbit to enter the core's Hill sphere in a single encounter ([Nishida 1983](#)). For orbits in this range we use the formalism of [Greenzweig and Lissauer \(1990, 1992\)](#) for gravitational stirring. For more distant orbits, the stirring rate is computed according to [Weidenschilling \(1989\)](#). Smaller separations are in horseshoe or Trojan-type orbits, and do not approach the core. Such bodies comprise a small fraction of the swarm's mass, and do not affect the core's evolution (they should not be identified with the present Trojan asteroids, which were probably captured subsequent to Jupiter's formation).

Planetesimals are brought to the vicinity of the core primarily by Keplerian shear, rather than by their random velocities. They encounter the core at a rate inversely proportional to their synodic period, or proportional to the difference in their semi-major axes. During an encounter, the velocity impulse imparted by the core is mostly in the plane of its orbit, so the stirring rate for inclinations is much less than for eccentricities. This effect tends to keep the planetesimal swarm relatively flat. Stirring within a swarm of comparably-sized bodies typically produces inclinations with magnitude about half that of eccentricities, but in the region within a few Hill radii of the core's semi-major axis, eccentricities are about an order of magnitude larger than inclinations. Planetesimals with nonzero eccentricities are able to enter the core's Hill sphere if their perihelia or aphelia are within $2.4R_H$ of the core's orbit. We compute the probability of collision with the core according to [Greenberg et al. \(1991\)](#). Appropriate expressions are used, depending on whether the thickness of the swarm (semi-major axis

times inclination) is larger or smaller than the Hill radius and/or the gravitationally enhanced collisional radius.

2.2. Evolution of the planetesimal swarm

We start the growth of Jupiter's core from a “seed” body embedded in a swarm of smaller planetesimals at Jupiter's present distance, $a = 5.2$ AU. The radial grid for the planetesimal evolution calculation extends from 4.7 to 5.75 AU. We impose the condition that the bodies in the outermost zone are not depleted due to gas drag; i.e., that the bodies in that zone are effectively replaced by bodies from farther out with the same size distribution. The nebula's surface density varies inversely with heliocentric distance; the value for the planetesimal swarm is $\sigma_Z = 10 (5.2 \text{ AU}/a) \text{ g cm}^{-2}$, giving an isolation mass (Lissauer 1987)

$$M_{\text{iso}} \approx 0.0026 \left(\frac{a}{\text{AU}} \right)^3 \left(\frac{\sigma_Z}{\text{g cm}^{-2}} \right)^{3/2} M_{\oplus} \quad (3)$$

of about $11 M_{\oplus}$, assuming a “feeding zone” of full width equal to $8 R_H$ (see Lissauer and Stewart 1993; Kary and Lissauer 1994), where the Hill radius is defined after Equation (2). The surface density of the gas at the seed's orbit is $\sigma_{XY} = 1000 \text{ g cm}^{-2}$, with density $3.3 \times 10^{-9} \text{ g cm}^{-3}$. The radial pressure gradient causes the gas to revolve about the proto-sun at $\sim 25 \text{ m s}^{-1}$ less than the local Keplerian velocity.

The initial swarm is assumed to consist of planetesimals with a power law size distribution from 15 m to 50 km in radius; the slope is the collisional equilibrium value of $-11/6$ (incremental mass), which places most of the mass in the largest bodies, tens of kilometers in radius or larger. Their bulk density is taken to be constant and equal to 1.4 g cm^{-3} , corresponding to a mixed rock/ice composition, with the mass of the largest planetesimals being $7.7 \times 10^{20} \text{ g}$. The planetesimal fragmentation model takes into account both a size-dependent material strength and the gravitational binding energy (Davis et al. 1994). For the smallest bodies, the material strength S decreases with increasing radius R due to the presence of defects in the solid material; we assume that $S(R)$ is proportional to $R^{-0.24}$ in this regime. At large sizes, self-compression increases strength, with $S(R)$ proportional to $R^{1.89}$. The minimum strength is $S = 1.9 \times 10^5 \text{ erg g}^{-1}$ at $R = 5 \text{ km}$. Impacts result in cratering or shattering of planetesimals. The impact strength essentially governs the size distribution of fragments. The amount of mass escaping is set by the ratio of the kinetic energy of the fragments to the impact energy in the center-of-mass frame. We assume a ratio of 1%, i.e., highly dissipative collisions. As most of the mass of the swarm is in planetesimals tens of kilometers in size, only a small fraction of the swarm mass is lost by collisional grinding down to radii $\lesssim 10 \text{ m}$. The results of the simulations are not sensitive to the strength of the planetesimals. All planetesimals striking the core are accreted.

The initial orbital eccentricity of the planetesimals is $\sim 1.7 \times 10^{-3}$, with the initial inclination half that value; these values give initial random velocities comparable to the escape velocity of the largest planetesimals. The initial values are not critical, provided they are low enough so that the initial accretion by the seed body is dominated by Keplerian shear, which allows the core to outgrow the other bodies. As runaway growth occurs, velocities near the core's orbit are dominated by its perturbations, not by

those of the bodies in the swarm. The core has a much lower eccentricity, $\sim 10^{-4}$, throughout the simulation.

The seed body has an initial mass of $5.7 \times 10^{23} \text{ g}$ ($10^{-4} M_{\oplus}$) and density 3.2 g cm^{-3} , for a radius of $\sim 350 \text{ km}$; the density of the growing planetary core remains constant throughout the simulation presented herein, with compression compensating for the accretion of lower density planetesimals. This roughly Ceres-sized body is sufficiently large compared with the neighboring planetesimals to initiate runaway growth. The initial conditions ensure that the growth of the core occurs in the regime dominated by Keplerian shear, with the swarm's thickness smaller than the size of its Hill sphere. This regime allows the most rapid “monarchical” growth (Weidenschilling 2005). Although other bodies in the simulation are allowed to grow, they are unable to overtake the core before its own perturbations stir eccentricities in the surrounding region and prevent runaway growth of potential competitors. In a typical simulation, the largest bodies other than the core reach sizes of a few hundred km in radius. We do not speculate on the origin of the seed body, which is more massive than its neighbors by three orders of magnitude. However, we note that such a body is more plausible than the Mars- or Earth-sized initial bodies assumed in many previous studies (e.g., Pollack et al. 1996; Dodson-Robinson et al. 2008; MBPL10).

We might expect the rapid growth of the core under these conditions would continue until it reached the isolation mass, $\sim 10 M_{\oplus}$. However, that limit is based on the idealized restricted three-body problem, in which there are no interactions among planetesimals and no non-gravitational forces. We find that inclusion of mutual collisions among the planetesimals and nebular gas drag affect the later stages of core growth, and may prevent it from reaching the theoretical isolation mass in Equation (3). If a planetesimal experiences a synodic encounter with the core that does not result in a collision, its eccentricity is typically increased. Conservation of the Jacobi parameter implies that its semi-major axis is also changed in such a manner as to increase its mean distance from the core; i.e., if its orbit is inside (outside) that of the core, its semi-major axis decreases (increases; see Nishida 1983). This effect occurs for synodic encounters at all distances, not just for planetesimals in the core's feeding zone; however, it is strongest near the core's orbit. In the absence of dissipation, the increase in the planetesimal's eccentricity allows a planetesimal capable of a close encounter with the core to make additional close approaches in future encounters. However, inclusion of damping, by collisions or gas drag, may reduce its eccentricity before the next synodic encounter. The net result is to push planetesimals away from the core (Greenberg 1983). This “shepherding” effect, in combination with the depletion of mass due to accretion, produces a gap in the swarm around the orbit of the growing core (Tanaka and Ida 1997). Note that this gap is only in the swarm of solid planetesimals; the planet does not typically produce a gap in the nebular gas until it approaches a mass of a few to several times $10 M_{\oplus}$, depending on nebular parameters, see D'Angelo et al. (2011); Lubow and Ida (2011).

Planetesimals pushed away by the core's perturbations pile up in the regions adjacent to the gap, increasing the local surface density of solids. This effect is partially offset by the secular decay of semi-major axes due to gas drag, on a timescale with order of magnitude given by Equation (1), as the radial pressure gradient causes non-Keplerian rotation of the nebula gas. Depending on their sizes and the nebula

lar parameters, small bodies migrating inward may pile up near the outer edge of the gap, or be fed to the core from that region. On the sunward side, the core's perturbations and drag act in the same direction, softening somewhat the edge of the gap. These effects can be seen in Figure 1, which illustrates the number of planetesimals for each zone in semi-major axis and for each size bin (left) and the surface density of solids versus semi-major axis (solid lines in the right panels). There are modest asymmetries in the planetesimal distribution with respect to the core's orbit (see, e.g., bottom left panel). The formation of a gap in the swarm about the orbit of the core, and its increasing width as the core grows, is clearly visible in the right panels, as is the local increase in surface density in the regions near the gap edges. The half-width of this gap is about $4 R_H$ when $M_c = 7 M_\oplus$. Since gas drag tends to smooth out the gap edges, they are less steep in the semi-major axis distribution of smaller bodies, as illustrated in the left panels by less sharp transitions for smaller R . Relative to the unperturbed (i.e., initial) distribution (dashed line in the right panels), in the bottom panel of the figure, an excess of approximately 0.12 and 0.25 M_\oplus worth of solids is collected at the inner and outer gap edge, respectively. As mentioned above, the asymmetry is due to the fact that gas drag causes inward drift of small planetesimals. Mass tends to pile up at the outer edge of the gap, where drag is opposed by the core's perturbations, while these two effects act in the same direction at the inner edge. It is worth noticing that the calculations presented here do not include the effects of planetesimals trapping into mean motion resonances with the planet.

The top and middle right panels of Figure 1 show double peaks around the gap edges. The bodies in these regions have non-negligible eccentricities due to repeated synodic encounters with the core. This can be seen in the left panels of Figure 2, which show the mean orbital eccentricities of planetesimals versus semi-major axis and size. The right panels of the figure show the mean orbital inclinations. We do not integrate individual orbits, but use a statistical estimate of the impact rate as a function of relative velocity and difference in semi-major axes from Greenzweig and Lissauer (1990) and Greenzweig and Lissauer (1992). The double peak (or rather, a single valley in the region of enhanced surface density produced by shepherding) is due to our algorithm for collision probability, which is maximized for orbits that are tangential to that of the target body. Those with perihelia or aphelia at a distance equal to the core's semi-major axis are depleted more rapidly, producing the local minima in surface density. It is not clear whether this is a real effect that would appear if the orbits were actually integrated, but it probably does not have a significant effect on the long-term evolution of the core mass.

As anticipated above, most of the mass of the swarm is placed in bodies with radii of tens of kilometers. In the distributions of planetesimals shown in the left panels of Figure 1, the single size bin that contains most mass, 10% of the total mass of the swarm at the time when $M_c = 1 M_\oplus$ and 14% when $M_c = 7 M_\oplus$, is that corresponding to radii $45 \lesssim R \lesssim 55$ km. In the distributions illustrated in the upper two panels, as can be seen from the cumulative mass fractions in Figure 3, less than 9% of the mass is in the form of planetesimals smaller than 1 km in radius, < 25% is in planetesimals with radii between 1 and 10 km, and < 2% is in planetesimals larger than 100 km in radius. Solids mass tends to be transferred to larger bodies as the swarm

evolves. In the bottom panel of Figure 1, only about 13% of the total mass is accounted for by planetesimals with radii $R \lesssim 10$ km and about 7% is accounted for by planetesimals larger than 100 km in radius (see Figure 3).

Pollack et al. (1996) assumed that the planet's feeding zone had a half-width of $\sqrt{12 R_H^2 + e^2 a^2}$, and that the planetesimals were distributed uniformly over the feeding zone. In our radially resolved simulations, the feeding zone is of comparable width, but the surface density is not uniform. Planetesimals near the edges of the feeding zone (more than about $2.4 R_H$ from the core's orbit) require many synodic encounters with the core before their eccentricities become large enough to cross its orbit and collide with it. Bodies whose semi-major axes are within $\sim 1 R_H$ of the core are in horseshoe or Trojan orbits, and are also initially unable to make close approaches to the core. Our multi-zone code can resolve the structure of the feeding zone. For a $5 M_\oplus$ core, the half-width is ~ 0.3 AU; we typically use a width of ~ 0.005 AU for each zone of semi-major axis. The initial rate of mass gain of the core is high due to shear-dominated runaway growth as it sweeps up planetesimals in the range ~ 1.8 – $2.4 R_H$, but decreases as this favored region of the feeding zone becomes depleted. The phase of rapid growth lasts until the core reaches about one-third of the isolation mass. Growth then continues at a slower rate, as planetesimals diffuse into the favored region of the feeding zone by collisions and nebular gas drag. In test simulations that do not include effects of a gaseous envelope captured by the core, this rate is so slow that the core cannot reach even half the isolation mass in Equation (3) during the lifetime of the nebula.

2.3. Growth of a bare core

Figure 4 shows the core mass versus time for our nominal simulation for the growth of a core *without* the gaseous envelope. Based on the initial mass-doubling timescale, it is assumed that the growth time of the initial seed body, from a size comparable to the largest bodies in the initial swarm, is about 5×10^4 years. Therefore, we set the time equal to 5×10^4 years at the beginning of the simulation.

In this model, the cross-section for accretion of planetesimals is equal to the geometrical cross-section of the core. The maximum rate of accretion, $\dot{M}_c \approx 1.3 \times 10^{-4} M_\oplus \text{ yr}^{-1}$, occurs when the core mass is around $1.5 M_\oplus$, and the rate steadily declines afterward (except for sporadic fluctuations, see Figure 8). The core only grows to a mass of about $4.4 M_\oplus$ in a little over 1 Myr. At the end of the calculation, the accretion rate is $\approx 3 \times 10^{-7} M_\oplus \text{ yr}^{-1}$. Even if the accretion rate leveled off at this time, the core would reach a mass of $\approx 5 M_\oplus$ at a time of 2.7 Myr and would not attain half of the isolation mass in Equation (3) until 4.3 Myr had elapsed. In fact, at the end of the calculation, the decline of \dot{M}_c as a function of the core mass is so steep that, were it to continue at a comparable rate, a further 10% increment of M_c would require an additional ~ 5 Myr.

The effective mass limit of the planet in this case probably depends somewhat on the size distribution of the planetesimals, their impact strength, the fragmentation model, and the nebular gas density. Additional details on the bare core calculation are presented in Section 4.

2.4. Effects of a gaseous envelope on accretion of the core

The later stage of accretion can be aided by effects of a gaseous envelope of hydrogen/helium captured from the

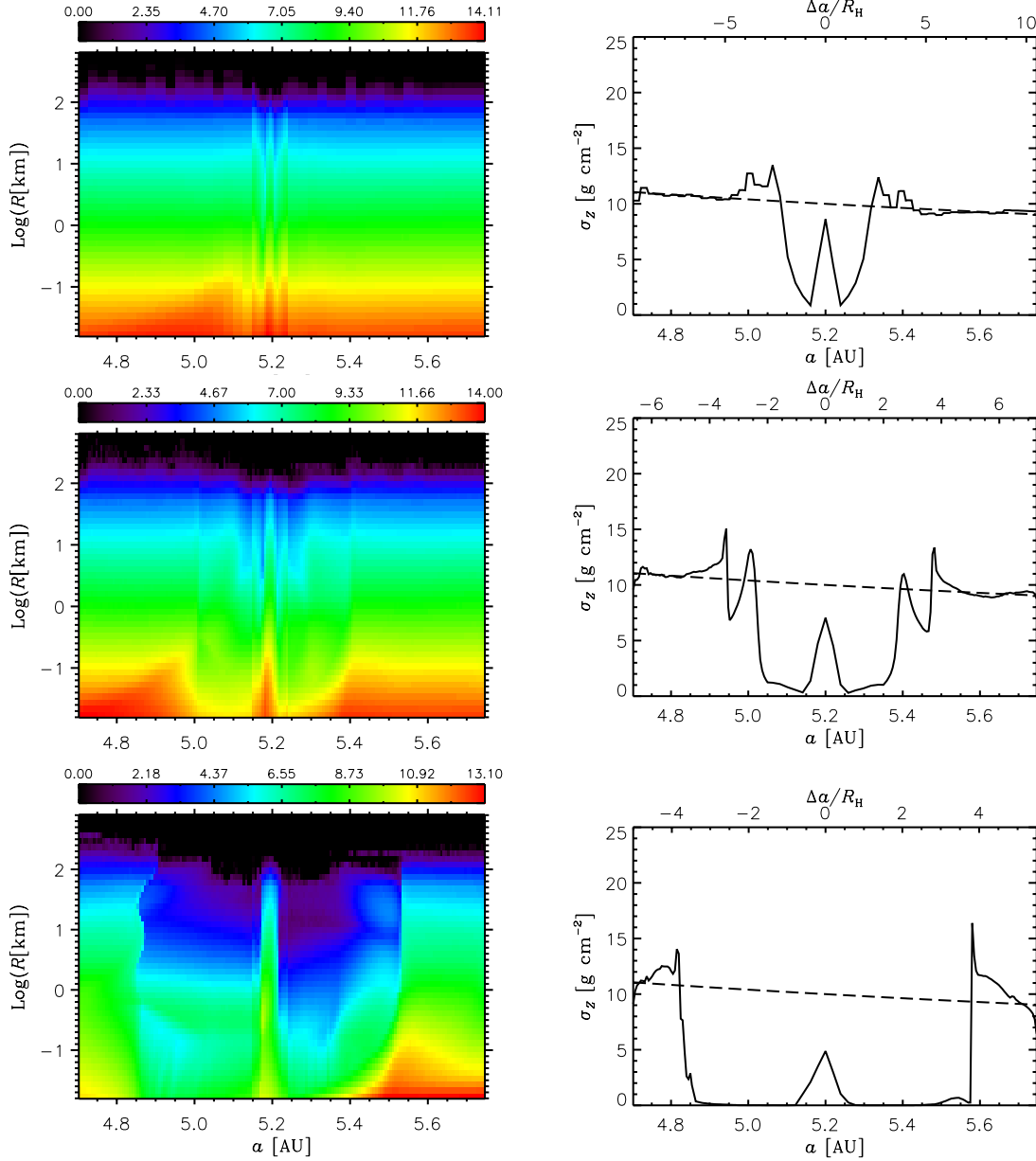


Fig. 1. Left. Planetesimal distributions as a function of semi-major axis and radius. Each plot shows the logarithm (in base 10) of the number of bodies per radial zone and size bin. From top to bottom, the distributions are plotted when $M_c = 1, 3$, and $7 M_\oplus$. Right. Cumulative surface density per surface zone (solid lines), computed as the total planetesimal mass divided by the surface area of the zone. The dashed line represents the initial surface density of solids, which scales as $1/a$. The top axis of each panel gives the distance from the planet in units of the planet Hill radius. These plots clearly show the formation and widening of the gap in the swarm around the orbit as the planet grows.

nebula and retained by the planet's gravity. The core begins to acquire an envelope significantly denser than the surrounding nebular gas when it attains a mass typically $\gtrsim 0.1 M_\oplus$. We compute the mass and structure of such an envelope by the method described in the next section. In our simulation with an envelope, the cross-section of the core for planetesimal capture during close encounters is augmented by drag exerted by the denser gas of the surrounding envelope. The cross-section is calculated self-consistently by solving for the structure of a quasi-hydrostatic envelope that grows in mass as it contracts. The capture cross-section for planetesimals becomes a function of both size and approach velocity. Small planetesimals that encounter the denser gas surrounding the core are braked by aerodynamic drag, and may also be disrupted by dynamical pressure, while larger bodies may pass through the outer region of the envelope

without being affected much. By the method described in the next section, we find that initially the effective collision radius of the largest planetesimals, with diameters of a few hundred km, is comparable to the physical radius of the solid core, R_c . But once the envelope mass grows beyond $\sim 10^{-3} M_\oplus$, the capture radius of the largest bodies can become significantly larger than R_c . For the smallest bodies, a few tens of meters in size, the effective collision radius may exceed R_c by an order of magnitude or more. While the swarm is flat compared with the Hill radius, the collision radius for bodies entering the Hill sphere is much smaller, so the collision cross-section varies as its square. Thus, the presence of the envelope can increase the accretion rate of small bodies onto the core by two, or more, orders of magnitude.

The presence of the envelope also affects the gravitational

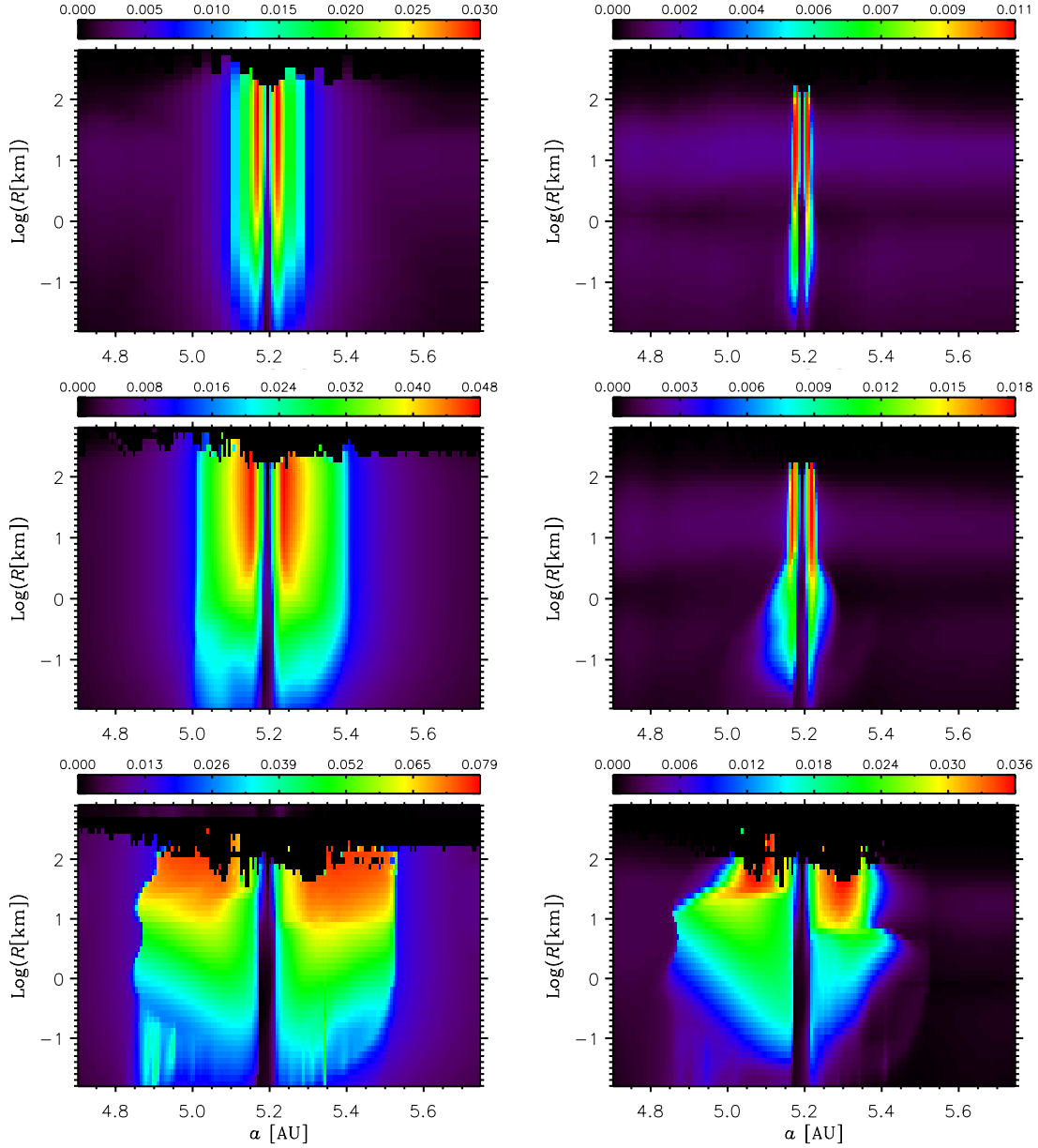


Fig. 2. Distributions of mean orbital eccentricities (left) and of mean orbital inclinations (right) of planetesimals as a function of semi-major axis and radius. From top to bottom, the distributions are plotted when $M_c = 1, 3$, and $7 M_{\oplus}$. The right panels actually show the sine of the mean inclinations.

stirring rate. Its mass added to that of the solid core increases the effective stirring. In the early stages of core growth, the envelope mass is only a small fraction of the total, and has little direct effect. However, there is another subtle effect, as the stirring rate depends on the closest approach distance that results in deflection without collision. The enhanced collision cross-section increases the lower limit for such encounters, decreasing the stirring rate, particularly for the smaller planetesimals. Another way to describe this effect is that the small planetesimals that approach the core are selectively removed by accretion, rather than stirred by such encounters. This process effectively diminishes the stirring rate, cooling the swarm. We compute the envelope structure and cross-section for planetesimal capture for each size bin, as outlined in the following sections.

2.5. Envelope structure calculation

The envelope surrounding the growing core is described by the typical equations of stellar structure (e.g., Kippenhahn et al. 2013), with the additional energy source provided by the gravitational energy of incoming planetesimals. These equations are solved using the 1-D code described in Pollack et al. (1996); Bodenheimer et al. (2000); Hubickyj et al. (2005), with modification described below in Section 2.6. The gaseous envelope is supposed to have a protosolar ratio of hydrogen and helium with a small admixture of heavier elements. In the following, we shall refer to this part of the model simply as the envelope evolution calculation, as opposed to the core accretion calculation described above.

Along with the module for the calculation of the envelope structure, the code includes three other main modules. The first module deals with the calculation of the interaction of the accreted planetesimals with the gas in the envelope, in-

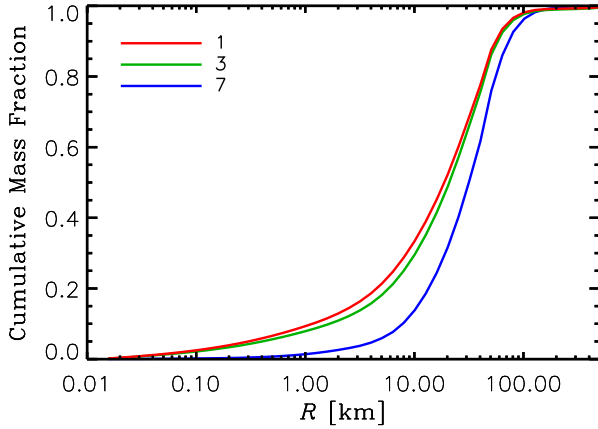


Fig. 3. Cumulative mass of the planetesimal distributions obtained by integrating the data plotted in the left panels of Figure 1 over semi-major axis and then integrating from the minimum planetesimal radius to R . The curves are normalized to the total mass in the distribution. The three curves refer to the times when $M_c = 1, 3$, and $7 M_\oplus$, as indicated in the legend.

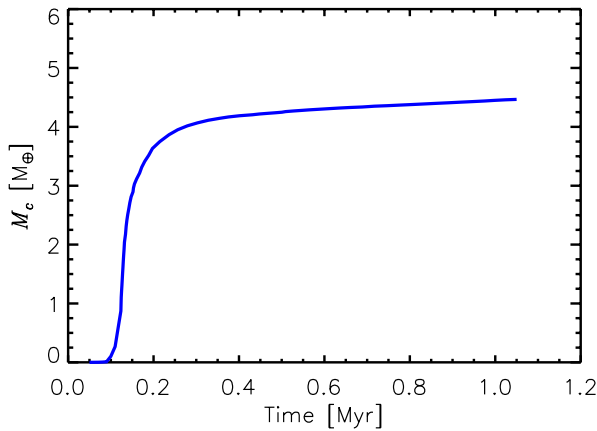


Fig. 4. Core mass versus time in a simulation that does not take into account the enhancement of the cross-section for collisional capture of planetesimals caused by the gaseous envelope bound to the core. In 1 Myr, the core grows to a mass that is only about 40% of that expected according to the standard concept of isolation mass (Equation 3). The maximum accretion rate is $\approx 1.3 \times 10^{-4} M_\oplus \text{ yr}^{-1}$. Toward the end of the calculation, \dot{M}_c is about $3 \times 10^{-7} M_\oplus \text{ yr}^{-1}$ and a steeply declining function of M_c .

cluding the computation of trajectories and ablation rates of the planetesimals as they travel through the envelope. The second module calculates, in a self-consistent fashion, the opacity at each depth in the envelope, accounting for sedimentation and coagulation of dust and small grains that are released in the envelope by ablating planetesimals, as described by MBPL10. The third module performs the calculation of the accretion of nebular gas on the envelope, which includes the calculation of the limiting rates² of accretion at which the nebula can supply gas to the planet as described by Lissauer et al. (2009).

The location of the inner boundary of the envelope is at the core radius, R_c . Prior to the phase of rapid envelope

contraction (or runaway gas accretion), the location of the outer boundary of the envelope, i.e., the planet radius R_p , is required to match the accretion radius. Based on thermal escape considerations and 3-D hydrodynamics disk-planet interaction calculations, the inverse of the accretion radius, $1/R_A$, is set equal to the sum

$$\frac{1}{R_A} = \frac{1}{R_B} + \frac{4}{R_H}, \quad (4)$$

where R_B and R_H are the Bondi and Hill radius, respectively. The factor 4 in the equation comes from an estimate of the volume in which the 3-D flow is bound to the planet (Lissauer et al. 2009). During this stage, density and temperature at R_p are those of the ambient nebula gas, ρ_{neb} and T_{neb} , respectively.

2.6. Planetesimal-envelope interaction and capture radii calculation

Planetesimals that travel through the hydrogen/helium envelope can lose a significant amount of kinetic energy if acted upon by a large enough drag force. The rate of change of the kinetic energy of a planetesimal as a result of the work performed by gas drag is

$$Mv\dot{v} = -\frac{1}{2}\pi R^2 \rho v^3, \quad (5)$$

where R is the planetesimal radius, v its velocity relative to the gas, M the planetesimal mass, and ρ the gas density. The drag coefficient is assumed to be 1. By solving for the velocity, we find that $1/v = \pi R^2 \rho t / (2M)$ plus a constant. This implies that a 30% loss in velocity, or a 50% loss in the kinetic energy, requires that the planetesimal travel through a mass of gas, $\pi R^2 \rho v t$, about equal its own mass, M . Considering that the interaction occurs over a length of at most $\sim R_p$, this condition also requires that the gas-to-planetesimal density ratio exceed the ratio $\sim R/R_p$. These simple arguments neglect the increase of the gas density within the planet's envelope and the mass reduction of the planetesimal through ablation. Therefore, they underestimate the radius of captured bodies. In fact, the condition $\pi R^2 \rho v t \approx M$ is clearly aided by an increasing ρ and a decreasing M .

The numerical module that calculates the interaction between an incoming planetesimal and the core's envelope was extended to allow for the application to a size distribution of planetesimals. The equations of motion account for the gravity force of the core and the envelope, and for gas drag following the formalism of Podolak et al. (1988). A sequence of trajectory integrations with impact parameter varying from zero to R_p is attempted. The integration also takes into account the mass loss of a planetesimal as it dissolves via ablation. The effective collision radius, or capture radius R_{capt} , is given by the largest impact parameter for which the planetesimal does not have enough (relative) kinetic energy to escape into heliocentric orbit, after one pass through the envelope.

After the determination of R_{capt} , the calculation proceeds by performing a number of trajectory integrations, with impact parameter varying between zero and R_{capt} , in order to determine and record the ablation history of a planetesimal, or whether it breaks up before hitting the core, for each impact parameter. This is done for all planetesimal sizes in the distribution, following the approach of Podolak et al. (1988) to calculate the thermal balance at the surface

² These limiting rates, at a heliocentric distance of 5.2 AU, typically set in only when the planet mass grows beyond several dozen Earth masses.

of the body and the ablation rates. Along its path in the envelope, a planetesimal can be completely ablated, break up, or hit the core. Averages over the various trajectories (with differing impact parameter) provide the mean energy and mass deposited in the envelope at each depth. The deposition of energy contributes to the energy budget of each envelope layer, whereas the mass deposited represents the input for the dust sedimentation and coagulation calculation, which includes the calculation of dust opacity. The ablated mass is supposed to eventually settle at the bottom of the envelope and is added to the core mass. Notice, however, that this assumption is valid for the rocky component of the solids, while ices can dissolve in the envelope (Iaroslavitz and Podolak 2007). Future work will take into account the effects of the dissolved ice in the envelope outer layers.

The numerical integrator for the calculation of trajectories was upgraded to a fifth-order Dormand-Prince method with an adaptive step-size control based on the global accuracy of the solution (Hairer et al. 1993). Convergence of the solution is obtained within a relative tolerance of 10^{-5} or an absolute tolerance of 10^{-10} , whichever is achieved first.

2.7. Solids accretion calculation with envelope-enhanced capture radii

The accretion of the core from the planetesimal swarm begins when $M_c = 10^{-4} M_\oplus$. Gas can become bound to the core only when the escape velocity from the core exceeds the mean thermal velocity of the ambient gas. Otherwise stated, it is necessary that the Bondi radius R_B is sufficiently larger than the radius of the core. At Jupiter's orbital distance ($T_{\text{neb}} \approx 120$ K), this condition typically requires a core whose mass is $\sim 0.1 M_\oplus$. However, around such a small core, most of the envelope would have a density on the order of the nebula density, and therefore $R_{\text{capt}} \sim R_c$ for all but meter-size planetesimals. Consequently, at the beginning of the evolution, we neglect the effects of the tenuous atmosphere that may form around the low-mass core ($M_c \leq 1 M_\oplus$).

We initialize the model as follows. Let us indicate with $i = 1, \dots, N$ the size bins in the swarm of planetesimals. We follow the growth of the seed body until it becomes a planetary core with mass $M_c = 1.1 M_\oplus$ (see Figure 4), applying capture radii $R_{\text{capt}}(i) = R_c$ and generating the solids' accretion rates, $\dot{M}_c(i)$ (see Section 2.2). At this point, we start the calculation of the envelope structure (the envelope mass is $M_e \sim 10^{-5} M_\oplus$), applying the accretion rates $\dot{M}_c(i)$ computed at $M_c = 1.1 M_\oplus$ and producing the envelope-enhanced capture radii, $R_{\text{capt}}(i)$, for each planetesimal radius, according to the procedure outlined in Section 2.6. The capture radii are also “centered” in core mass at $M_c = 1.1 M_\oplus$. The envelope-enhanced capture radii are then used to update and evolve the core accretion calculation from $M_c = 1.0$ to $1.2 M_\oplus$. As mentioned above, the envelope mass is also taken into account in the core accretion calculation. At the end of the initialization procedure, we have solids' accretion rates computed for $M_c = 1.2 M_\oplus$, based on capture radii computed for $M_c = 1.1 M_\oplus$. The envelope evolution and core accretion calculations are staggered in core mass by an amount equal to $\Delta M_c = 0.1 M_\oplus$.

The overall calculation proceeds in a step-wise fashion, by advancing the envelope evolution and core accretion calculations so that the core mass increases by $\Delta M_c = 0.2 M_\oplus$ in each step, and exchanging data ($\dot{M}_c(i)$, $R_{\text{capt}}(i)$, and M_e)

between the two calculations at the end of each step. As a result, in advancing from M_c to $M_c + \Delta M_c$, each calculation employs information from the other calculation computed at $M_c + \Delta M_c/2$.

We find that this procedure yields maximum variations of $\dot{M}_c(i)$, from one step to the next, of less than about 25% and even smaller maximum variations of $R_{\text{capt}}(i)$. As the planet mass grows, the gas accretion rate, \dot{M}_e , increases, eventually causing significant variations of the capture radii from one step to the next (smaller bodies may be especially sensitive to variations of the envelope mass, as explained in Section 2.4). Therefore, within an envelope evolution step, if the maximum variation of $R_{\text{capt}}(i)$ with respect to i exceeds 15%, we update $\dot{M}_c(i)$ by repeating the last core accretion step and applying the latest values computed for $R_{\text{capt}}(i)$ and \dot{M}_e . In addition, once gas accretion dictates planet growth, that is $\dot{M}_e > \dot{M}_c = \sum_1^N \dot{M}_c(i)$, the data exchange between calculations is executed at mass intervals $\Delta M_c = 0.05 M_\oplus$. However, the condition $\dot{M}_e > \dot{M}_c$ also marks the end of Phase 1 and the beginning of Phase 2 of the planet evolution (see Section 1), which will be described in a forthcoming paper.

2.8. Model improvement via a predictor-corrector scheme

The determination of the accretion rates of solids is affected by stochastic variations, for example, of the number of impacts on the core, which may add a random component to the physical variations of $\dot{M}_c(i)$, from one step to the next, in the scheme outlined above. In order to compensate for such effects, we can consider the calculation described so far as a “predictor” approximation of a predictor-corrector scheme.

The corrected calculation proceeds as follows. Indicating with $\dot{M}_c^k(i)$, for $k = 1, \dots, K$, the values of $\dot{M}_c(i)$ for increasing total planet mass, M_p^k ($M_p = M_c + M_e$), we reduce stochastic variations over small changes of M_p by introducing smoothed values of the accretion rate for each size bin

$$\langle \dot{M}_c \rangle_i^k = \frac{1}{3} [\dot{M}_c^{k-1}(i) + \dot{M}_c^k(i) + \dot{M}_c^{k+1}(i)]. \quad (6)$$

The edge values are defined as $\langle \dot{M}_c \rangle_i^1 = [2\dot{M}_c^1(i) + \dot{M}_c^2(i)]/3$ and $\langle \dot{M}_c \rangle_i^K = [\dot{M}_c^{K-1}(i) + 2\dot{M}_c^K(i)]/3$. Notice that the smoothing operator is globally conservative, in the sense that

$$\sum_{k=1}^K \langle \dot{M}_c \rangle_i^k = \sum_{k=1}^K \dot{M}_c^k(i), \quad (7)$$

as can be easily checked by direct substitution.

Equation (6) is applied to all the accretion rates' datasets used in the “predictor” calculation. We then build continuous functions of the planet mass $\langle \dot{M}_c \rangle_i = \langle \dot{M}_c \rangle_i(M_p)$ by performing linear interpolations of the smoothed accretion rates, $\langle \dot{M}_c \rangle_i^k$. The corrected calculation is obtained by restarting the envelope evolution from the beginning ($M_c = 1.1 M_\oplus$) and using the functions $\langle \dot{M}_c \rangle_i$ as accretion rates.

Figure 5 shows the total accretion rate used in the “predictor” step, \dot{M}_c (step function), as well as that used in the corrected calculation, $\langle \dot{M}_c \rangle$ (continuous function). We find that the smoother behavior of the accretion rate in solids leads to a smoother increase of the envelope mass, espe-

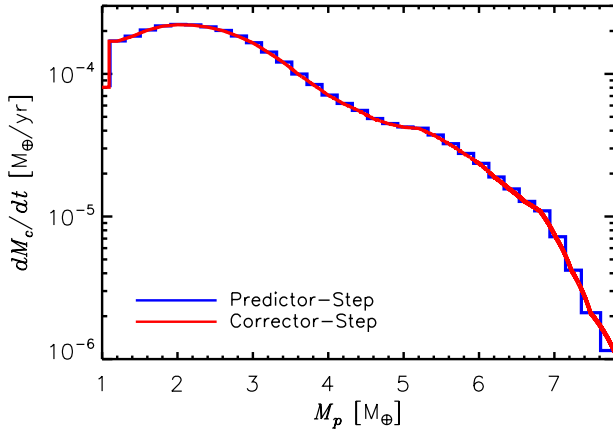


Fig. 5. The plot shows the accretion rate of solids $\dot{M}_c = \sum_i \dot{M}_c(i)$ (step function) applied in the “predictor” calculation (see Section 2.8) versus the planet mass, $M_p = M_c + M_e$. The quantity $\dot{M}_c(i)$ indicates the accretion rate for a given planetesimal radius in the size distribution. The smooth line represents the accretion rate $\langle \dot{M}_c \rangle = \sum_i \langle \dot{M}_c \rangle_i$, applied in the “corrector” calculation.

cially when \dot{M}_c changes by more than $\sim 30\%$ from one step to the next. We also find that the capture radii computed in the corrected calculation are very similar to those used in the “predictor” calculation (differences are within a few percent), for which reason a corrected version of the core accretion calculation is not performed.

In the rest of the paper, we will only refer to the corrected calculation. Therefore, for ease of reading, the notation $\langle \dot{M}_c \rangle$ will be dropped, and the accretion rate of solids is simply denoted as \dot{M}_c .

3. Comparison of the method with previous work

The analytic and statistical calculations of Kobayashi et al. (2010, 2011) provide planetesimal accretion rates that include collisional fragmentation and a range of planetesimal sizes, with the details somewhat different from those used here. The atmospheric enhancement of the planetesimal capture cross-section is included, with a more approximate atmospheric structure and effective capture radius than those described in Sections 2.5 and 2.6. The opacity calculation does not include grain settling and coagulation but rather assumes interstellar grain opacities multiplied by an arbitrary factor. They found that a disk with ten times the solid surface density of the minimum-mass solar nebula and an initial planetesimal size of 100 km (or larger) are required to generate a solid core of $10 M_\oplus$ in less than 10^7 years between 5 and 10 AU. An additional requirement is that the grain opacity be reduced by a factor ≈ 100 compared with interstellar values.

Independent simulations by Benvenuto et al. (2009) and Fortier et al. (2009), based on the method described in Fortier et al. (2007), employ a detailed model envelope and a capture radius calculation similar to ours. However the core accretion rate is simplified in that it does not use a statistical simulation with the calculation of the evolution of the planetesimal size distribution, but rather assumes a size distribution fixed in time or, alternatively, a single size. The planetesimal velocities are calculated according to an assumed balance between the stirring by the embryo and the damping by gas drag. The grain opacities are interstellar. The initial mass of the embryo is about $10^{-2} M_\oplus$. Ben-

venuto et al. (2009) found that Jupiter, at a fixed distance of 5.5 AU in a disk with a solid surface density $\sigma_Z = 11 \text{ g cm}^{-2}$, about 3.3 times that expected in the minimum-mass solar nebula, can form in less than 1 Myr if most of the planetesimals are in the size range 30 to 100 meters. However, if most of the planetesimal mass is in the kilometer size range, formation times are longer, about 6 Myr. Fortier et al. (2009) performed a similar calculation. For Jupiter at 5.2 AU, with a single planetesimal size of 10 km, the formation time is 2.4 Myr for a σ_Z six times that of the minimum-mass solar nebula. If the size is increased to 100 km, the formation time is longer: 3.2 Myr for a σ_Z ten times that of the minimum-mass solar nebula. Clearly, the details of the assumed planetesimal size distribution have an important influence on the results (Guilera et al. 2011).

A completely different approach is taken by Levison et al. (2010). They do an N-body simulation starting with 5 embryos of $1 M_\oplus$ each, situated between 4.5 and 6.5 AU, embedded in a disk of planetesimals with solid surface density 6 times that of the minimum-mass solar nebula. The simulations include embryo-disk tidal interactions, collisional damping, planetesimal-induced migration, embryo atmospheres, gas drag, and fragmentation. In their models, it is difficult to grow embryos to 10 Earth masses. The embryos open up a gap in the planetesimal disk in their vicinity and do not grow to more than about $2 M_\oplus$. In a few exceptional cases, the outer embryos undergo rapid, planetesimal driven, outward migration, and can accrete to up to $30 M_\oplus$. Given the differences in various physical assumptions, the different formation timescales between the calculations of Levison et al. and the calculation presented herein are not surprising. Perhaps, the most important differences concern the inclusion of embryo migration and the number of growing embryos. We do not allow the growing core to drift in response to the nebula torques and to core-planetesimals interaction whereas the inclusion of this effect is one of the main motivations driving Levison et al.’s investigation. In addition, while we introduce in the swarm an initial seed of $10^{-4} M_\oplus$ (which is large enough to become the dominant embryo), they use 5 closely spaced embryos that are much larger in mass. Moreover, the swarm dynamics and the gaseous envelope of the embryos are also modeled quite differently.

Over the past few years, the importance of the accretion of small, centimeter-to-meter size, solids has been investigated (e.g., Ormel and Klahr 2010; Lambrechts and Johansen 2012; Morbidelli and Nesvorný 2012; Chambers 2014). Because of their size, these bodies are subjected to a strong aerodynamic drag force. According to Equation (1), corrected for an appropriate drag coefficient, the orbital radius of meter-size bodies at ~ 5 AU would significantly shrink over the orbital period. (Notice, however, that Equation (1) is derived under the assumption of a Keplerian-like orbit.) Therefore, these fragments should be continuously replenished via collisional comminution of planetesimals in order to represent a persistent source of accretion. Although such comminution is allowed in our simulation, the larger planetesimals have significant gravitational binding energy, and are not prone to disruption. As mentioned in Section 2.1, the total mass lost at small sizes ($< 15 \text{ m}$) is about 10% of the total mass of the swarm. Even if the core accreted the fragments exterior of its orbit with a 100% efficiency, the core mass would change only marginally (by about 10%). For accretion of small solids to be important

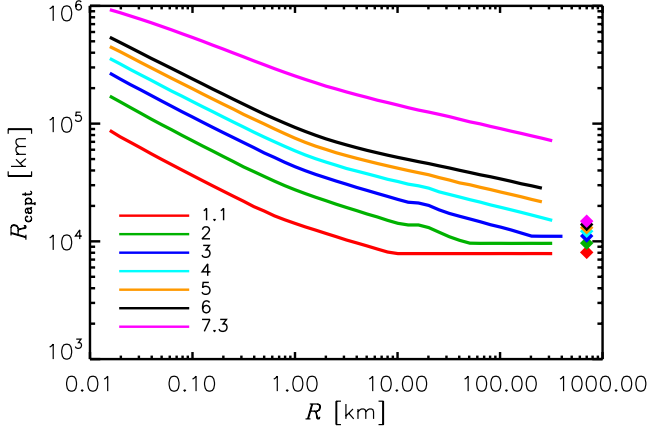


Fig. 6. The envelope-enhanced capture radius for planetesimal accretion versus planetesimal radius for different values of the core mass, M_c , in units of M_\oplus , as indicated in the legend. The symbols on the far right side of the diagram indicate the core radius, R_c . In the envelope around 1, 2, and $3 M_\oplus$ cores, larger planetesimals can reach the core and R_{capt} levels off to R_c . The inflection in the curves, around $R \sim 10$ km for $M_c = 2$ and $3 M_\oplus$, is caused by a regime transition between complete ablation and disruption.

in our simulation, we should have postulated that the initial planetesimals were much more fragile and prone to disruption, and/or that small bodies were abundant in the outer nebula and supplied more mass to the feeding zone than was originally present. But these scenarios are beyond the scope of the present investigation.

Furthermore, Chambers (2014) performed simulations of the oligarchic growth of giant planet cores including a populations of millimeter-to-meter size particles, which are produced by the collisional cascade initiated by larger (1–100 km size) planetesimals. He concluded that the importance for core accretion of these small particles depends on a balance between the production rate (via collisional comminution) and the loss rate (via drag-induced radial drift). If the parent population of planetesimals is constituted of objects of ~ 1 km in diameter, then the accretion rate in small particles is significant. However, if the parent planetesimals are large, ~ 100 km in diameter, then small particles do not provide a major source of solids accretion. In our calculation, most mass resides in large planetesimals, $\gtrsim 100$ km in diameter (see Section 2.2). Therefore, according to these findings, millimeter-to-meter size particles should not contribute significantly to the growth of the core in our calculation.

4. Results

As anticipated in the previous sections, the capture radius of the planet for planetesimal accretion, R_{capt} , is substantially enhanced by the presence of the gaseous envelope. Figure 6 shows R_{capt} versus planetesimal radius, R , for different core masses. At $\approx 1 M_\oplus$, the envelope mass is small, $\sim 10^{-5} M_\oplus$, yet planetesimals up to a few kilometers in radius are already affected by gas drag in the envelope so that $R_{\text{capt}} > R_c$. In fact, when $R = 4$ km, R_{capt} already exceeds the core radius by about 20%. For $R > 10$ km, R_{capt} is basically equal to R_c , as indicated by the symbols on the right side of the figure. When M_e grows to $10^{-4} M_\oplus$ ($M_c \sim 2 M_\oplus$), bodies up to 50 km in radius are affected by the envelope. Once the envelope mass exceeds $\sim 10^{-3} M_\oplus$ ($M_c \sim 4 M_\oplus$), the planet has a capture

radius larger than the core radius for essentially all planetesimals ($R_{\text{capt}}/R_c \approx 1.31$ for 250-km radius planetesimals and ≈ 1.24 for 320-km radius planetesimals). Around a core mass of about $6 M_\oplus$ and $M_e \sim 4 \times 10^{-3} M_\oplus$, the cross-section of the planet for accretion of 250-km radius planetesimals is 4 times as large as the geometrical cross-section. When $M_c = 7.3 M_\oplus$ ($M_e \approx 0.15 M_\oplus$), the cross-section for accretion of 320-km radius planetesimals exceeds the geometrical cross-section by a factor of over 20!

The accretion rate of solids by the planet versus planetesimal radius is plotted in Figure 7 (top panels), along with the cumulative distributions (bottom panels). Left and right panels correspond, respectively, to the calculation with and without envelope. In the latter calculation, $R_{\text{capt}} = R_c$ for all planetesimal in the swarm. Around the lowest core masses ($M_c \approx 1 M_\oplus$), $\dot{M}_c = \dot{M}_c(R)$ is affected by the planet's envelope mostly at small planetesimal radii, which results in accretion rates larger by factors of 5 at $R \approx 15$ m and about 2.5 at $R \approx 1$ km.

In absence of the envelope, there is a rapid drop of \dot{M}_c for $M_c \gtrsim 2 M_\oplus$ (see top-right panel, see also Figure 8), which instead becomes a gradual reduction when gas drag in the envelope is at work (see the top-left panel). Comparing distributions in the top panels, the accretion rates of the $3 M_\oplus$ core without envelope are comparable to those of the $6 M_\oplus$ core with envelope. In fact, the cumulative distributions show that the total accretion rate of the $3 M_\oplus$ bare core is similar (a 50% difference) to that of the $6 M_\oplus$ core with envelope. The $4 M_\oplus$ bare core has accretion rates very similar to those of the $7 M_\oplus$ core with envelope for radii $R \lesssim 1$ km and $R \gtrsim 100$ km. The peak accretion occurs at $R \approx 50$ km for both distributions, but it is less than 1/4 as large in the bare core calculation. The cumulative distributions in Figure 7 also indicate that about 10%, or less, of the accreted mass is in bodies smaller than 100 m in radius and about 70% is in bodies larger than 10 km. This last percentage varies somewhat, from $\approx 60\%$ for $M_c = 1\text{--}2 M_\oplus$ to $\approx 80\%$ for $M_c \gtrsim 6 M_\oplus$, possibly due to the transfer of mass from smaller to larger planetesimals as the swarm evolves (see Section 2.2). As explained below, the fact that most of the solids mass passing through the envelope is carried by large, 10 km-size bodies may have important consequences for the accretion of gas and the ultimate formation timescale. In fact, if most mass was contained in bodies of much smaller size, more dust would be deposited in the envelope and its opacity could be higher, inhibiting cooling and hence contraction.

A comparison among various calculations of solids and gas accretion rates, versus core mass, is presented in the top panel of Figure 8. The solid lines represent \dot{M}_c and the dashed lines \dot{M}_e . The red lines refer to the model discussed here. The blue and cyan lines show the results of models labelled as $\sigma 10$ ($\sigma_Z = 10 \text{ g cm}^{-2}$ at 5.2 AU) and $\sigma 6$ ($\sigma_Z = 6 \text{ g cm}^{-2}$ at 5.2 AU) of MBPL10. In those calculations, the solids accretion rates were based on the three-body problem accretion calculations of Greenzweig and Lissauer (1992), assuming a single-size planetesimals of 100 km in radius. The condition $\dot{M}_e \approx \dot{M}_c$ occurred at around the isolation mass given by Equation (3), respectively 11.5 and $5.6 M_\oplus$, whereas here the condition is realized prior to reaching that mass. However, in the present calculations, the concept of isolation mass (at least as stated in Equation (3)) does not strictly apply because of interactions among planetesimals and the effects of drag forces (see discussion Sec-

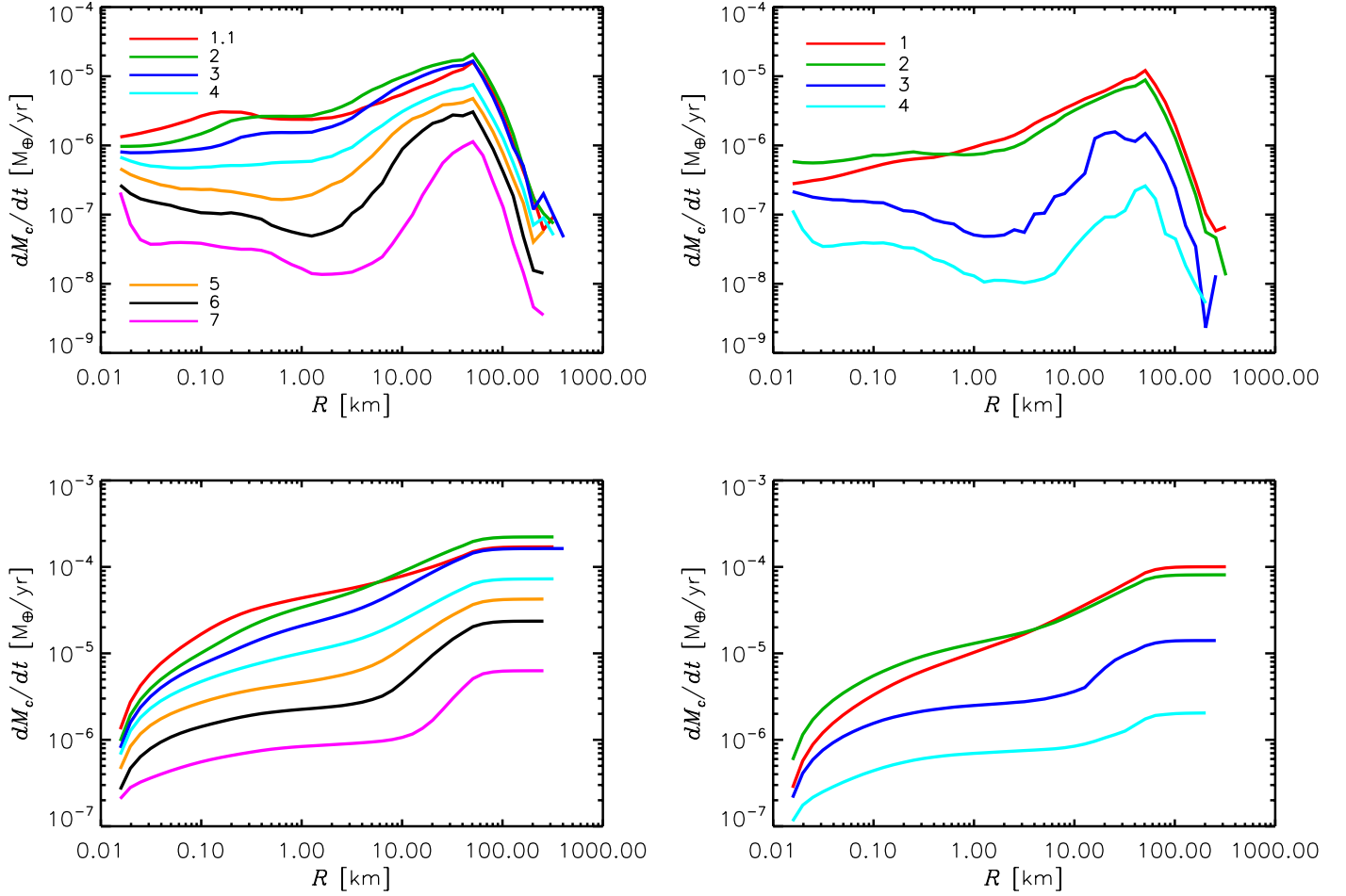


Fig. 7. The top-left panel shows the accretion rate of solids as a function of the planetesimal radius at various core masses, in units of M_{\oplus} , as indicated. The bottom-left panel shows the cumulative distribution of the accretion rate, at the same core masses, obtained from the curves in the top panel. For comparison, the same quantities are plotted in the right panels ($M_c = 1, 2, 3$, and $4 M_{\oplus}$) for the calculation of the growth of a core that does not have an envelope (see Section 2.2). Notice the large difference in \dot{M}_c between the left and right panels, especially for $M_c > 2 M_{\oplus}$, caused by gas drag in the growing planet's envelope.

tion 2.2).

Figure 8 (top panel) also shows, as a thin green solid line, \dot{M}_c for the case in which the enhancement of the cross-section for solids accretion due to the envelope is not included. Although the green and red lines have comparable peaks ($\approx 1.3 \times 10^{-4}$ and $\approx 2.2 \times 10^{-4} M_{\oplus} \text{ yr}^{-1}$, respectively) and the maximum of \dot{M}_c is reached at similar values of the core mass ($M_c \approx 1.5$ and $2.1 M_{\oplus}$), the presence of the envelope already accounts for a factor of 10 difference in \dot{M}_c at $M_c = 3.5 M_{\oplus}$ and a factor 100 difference at $M_c = 4.3 M_{\oplus}$. It is not trivial to predict the conditions for which the maximum of \dot{M}_c occurs. The accretion rate is mainly determined by the surface density of the planetesimal swarm, which is reduced by shepherding. The effectiveness of shepherding is a function of damping, which is due to two processes: collisions and gas drag. The rate of collisional damping depends on both the surface density of the swarm and the size distribution of the bodies, while the gas drag term depends on the size of an individual body and on the local gas density. However, the capture radius for accretion of 10 km-radius (and larger) planetesimals, which contribute most of the accreted mass (see Figure 7), begins to be affected by the gaseous envelope at core masses between 1 and

$2 M_{\oplus}$. Therefore, somewhat different values of M_c at which the accretion rates peak (and the maximum values) in the calculations with and without envelope are expected.

The luminosity of the planet as a function of the core mass is shown in the bottom panel of Figure 8 for the same models as in the top panel, except for the calculation without the envelope. The release of potential energy by both envelope contraction and solids accretion represents the source of planet luminosity. However, during these early phases of growth, most of the luminosity is provided by accretion of solids. In fact, the luminosity peaks in the figure closely follow the peaks in \dot{M}_c . In the current calculation, the maximum of the luminosity occurs ≈ 2000 years later than the maximum of the solids accretion.

The temporal evolution of both core and envelope mass may differ quite substantially from that of previous calculations that do not simulate the evolution of the planetesimal swarm, as illustrated in Figure 9. For example, despite having the same solids surface density at 5.2 AU, M_c in model $\sigma 10$ of MBPL10 grows much more rapidly, as \dot{M}_c starts to decrease only when $M_c \gtrsim 8 M_{\oplus}$, reaching $\approx 12 M_{\oplus}$ after 0.4 Myr (using the synchronization of Figure 9, left panel). At this point of the evolution, the ≈ 1.6 factor

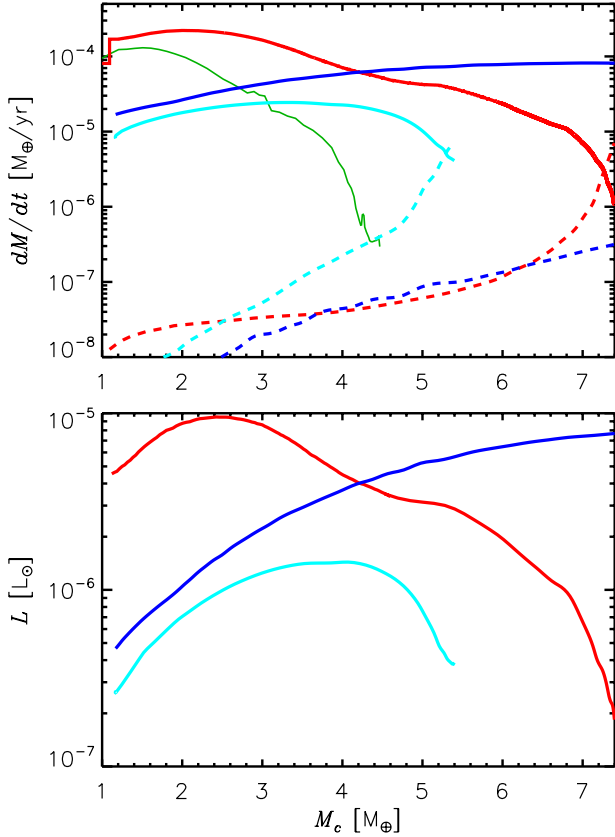


Fig. 8. Top: Accretion rate of solids (red solid line) and of gas (red dashed line) as function of the core mass according to the Jupiter formation model presented herein. The blue and cyan lines show the results for same quantities obtained, respectively, from models $\sigma 10$ and $\sigma 6$ of MBPL10 (see also Figure 9). The thin green solid line represents the accretion rate of solids for our calculation that does not account for the enhancement of the effective collision radius of planetesimals due to the presence of the envelope around the core (see discussion in Section 2.2 and Figure 4). The accretion rates plotted here are averaged over time intervals of 10^3 – 10^4 years. Bottom: Planet luminosity versus core mass for the cases corresponding to the models in the top panel (luminosity is not available for the bare core calculation).

difference in core mass is reflected by a similar fractional difference in the envelope mass, $\approx 1 M_\oplus$ against $0.57 M_\oplus$. There are some similarities to the $\sigma 6$ model of MBPL10 in that the core mass differs by about $2 M_\oplus$ (a $\approx 30\%$ difference) after 0.4 Myr and the envelope mass is only somewhat smaller than in the previous calculation ($M_e \approx 0.46 M_\oplus$). The larger M_e of the $\sigma 6$ model for equal core masses (and $M_c \gtrsim 2.5 M_\oplus$, see Figure 8), is a result of the lower solids accretion, which favors the contraction of the envelope on shorter timescales.

In Figure 10, we plot the temperature (top) and density (bottom) structure of the envelope for different values of the core mass. The temperature plateau at ~ 2000 K is the result of low molecular opacity (see the drop of κ in Figure 11) and low density ($\rho \lesssim 10^{-6} \text{ g cm}^{-3}$) at temperatures just above the evaporation temperature of the dust. Dissociation of molecular hydrogen may also contribute somewhat, as indicated by the line marks beneath the curves in the bottom panel. The vertical line segments correspond to the radii at which significant dissociation begins: the density ratio of atomic to molecular hydrogen is $\gtrsim 0.01$ to the left of the line marks. This temperature plateau is absent at

$M_c = 7.3 M_\oplus$ mainly because of the higher gas densities in that region ($\rho \sim 10^{-4} \text{ g cm}^{-3}$), resulting in higher molecular opacities and a higher optical thickness of that envelope layer. In fact, at this core mass, Figure 11 indicates that there is no opacity drop around 2000 K. In addition, at those densities, significant dissociation of molecular hydrogen begins at higher temperatures, as shown by the corresponding line segment in the bottom panel. The change in temperature gradient around 700 K in the $M_c = 7.3 M_\oplus$ case, at distances between 1.5 and $3 \times 10^5 \text{ km}$, appears associated with a low opacity around those locations (see Figure 11). The opacities at distances of $\sim 10^5 \text{ km}$ ($400 \lesssim T \lesssim 1500 \text{ K}$) come primarily from the dust, and the drop visible between core masses of 5 and $7.3 M_\oplus$ likely occurs partly because of the decline in \dot{M}_c , which causes less solid material to be delivered in those envelope layers. Moreover, because of the increase in envelope mass, planetesimals are ablated higher up in the envelope and so grains have more time to coagulate before they settle to those deeper layers, thus reducing the opacity.

The envelope structure surrounding cores with mass $1.1 \lesssim M_c \lesssim 6.3 M_\oplus$ are composed of two convective shells separated by a radiative shell. The arrowhead symbols in the top panel of Figure 10 mark the radial boundaries between convective and radiative layers, pointing in the direction in which the radiative zones extend. The outer radius of the interior convective zone increases as the core and envelope mass grow. The inner radius of the exterior convection zone also expands outward. Nonetheless, when $M_c \approx 6.3 M_\oplus$ ($M_e \approx 6 \times 10^{-3} M_\oplus$), the outer convection shell still occupies over 99.9% of the envelope volume (corresponding to 30% of the mass of the envelope). As M_c and M_e increase further, the outer layers become radiative. At $M_c \approx 7.3 M_\oplus$, there are two convective and two radiative zones of which the outermost (radiative) zone occupies 96% of the envelope volume (comprising 10% of the mass).

Simple arguments based on dissipation of kinetic energy via gas drag suggest that the path of a body traveling through gas is significantly affected once it encounters a mass of gas about equal to its own mass (see Section 2.6). Thus, assuming a traveling distance in the envelope on the order of the envelope radius R_p (i.e., $R_{\text{capt}} \ll R_p$), captured planetesimals have radii $R \sim (\rho/\rho_s)R_p$, where ρ is an average envelope density and ρ_s the density of the body. For small objects, the traveling distance is $R_p - R_{\text{capt}}$ and one should iterate the relation $R \sim (\rho/\rho_s)(R_p - R_{\text{capt}})$. Gas densities corresponding to the envelope around a $7.3 M_\oplus$ core imply that $\sim 100 \text{ km}$ size planetesimals may be captured at a distance of $\sim 8 \times 10^4 \text{ km}$. Planetesimals of ~ 10 and $\sim 1 \text{ km}$ in size may be captured at about 1.5 and 2.5 times that distance, respectively. These numbers agree within factors of order unity with the capture radii shown in Figure 6, but in reality the situation is more complex. In fact, planetesimal capture results from the combined effects of kinetic energy dissipation and mass loss due to ablation. As a body sheds mass, dissipation of energy by drag is facilitated.

For a given material, the mass loss of a body via ablation is proportional to its surface (see, e.g., Podolak et al. 1988). For an amount of solids ΔM traveling through an envelope layer during a time interval Δt , the mass ablated, ΔM_{ab} , is proportional to the total surface area exposed by the solids. Therefore, the ratio $\Delta M_{\text{ab}}/\Delta M$ is proportional to the total surface to volume ratio, i.e., to $1/R$ assuming a single size distribution of bodies with radius R . This implies that, for

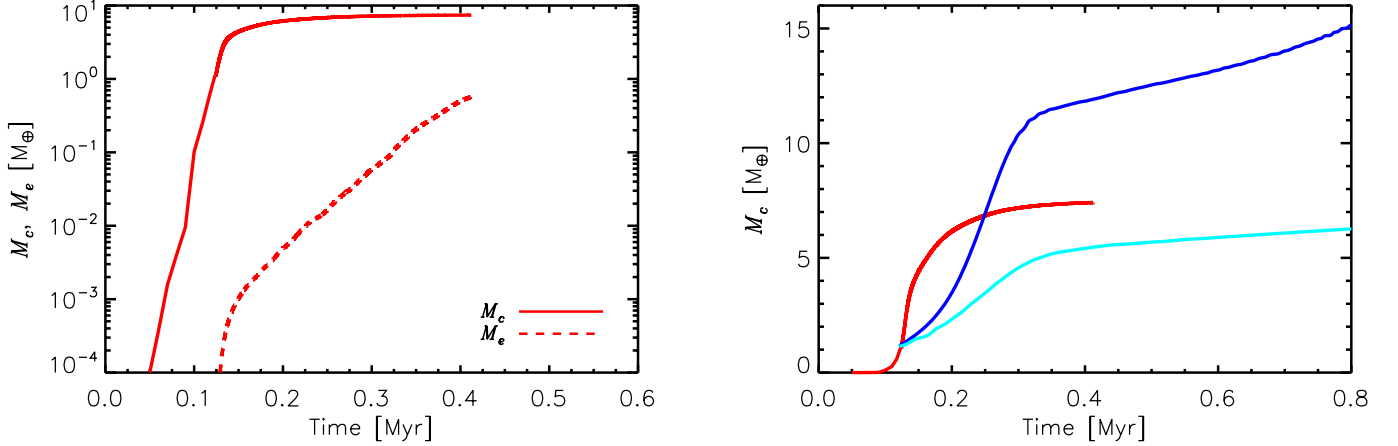


Fig. 9. Left: Core (M_c) and envelope mass (M_e) versus time in the current calculation. Right: Core mass growth for various models. The red line represents the current model (the same as in the left panel). The blue and cyan lines show the evolution in models $\sigma10$ and $\sigma6$ of MBPL10 (see also Figure 8), based on the solids accretion rates of [Greenzweig and Lissauer \(1992\)](#) and a single-size distribution with planetesimals of 100 km in radius. These last two models are time shifted so that $M_c \approx 1.1 M_\oplus$ at approximately the same time for all curves.

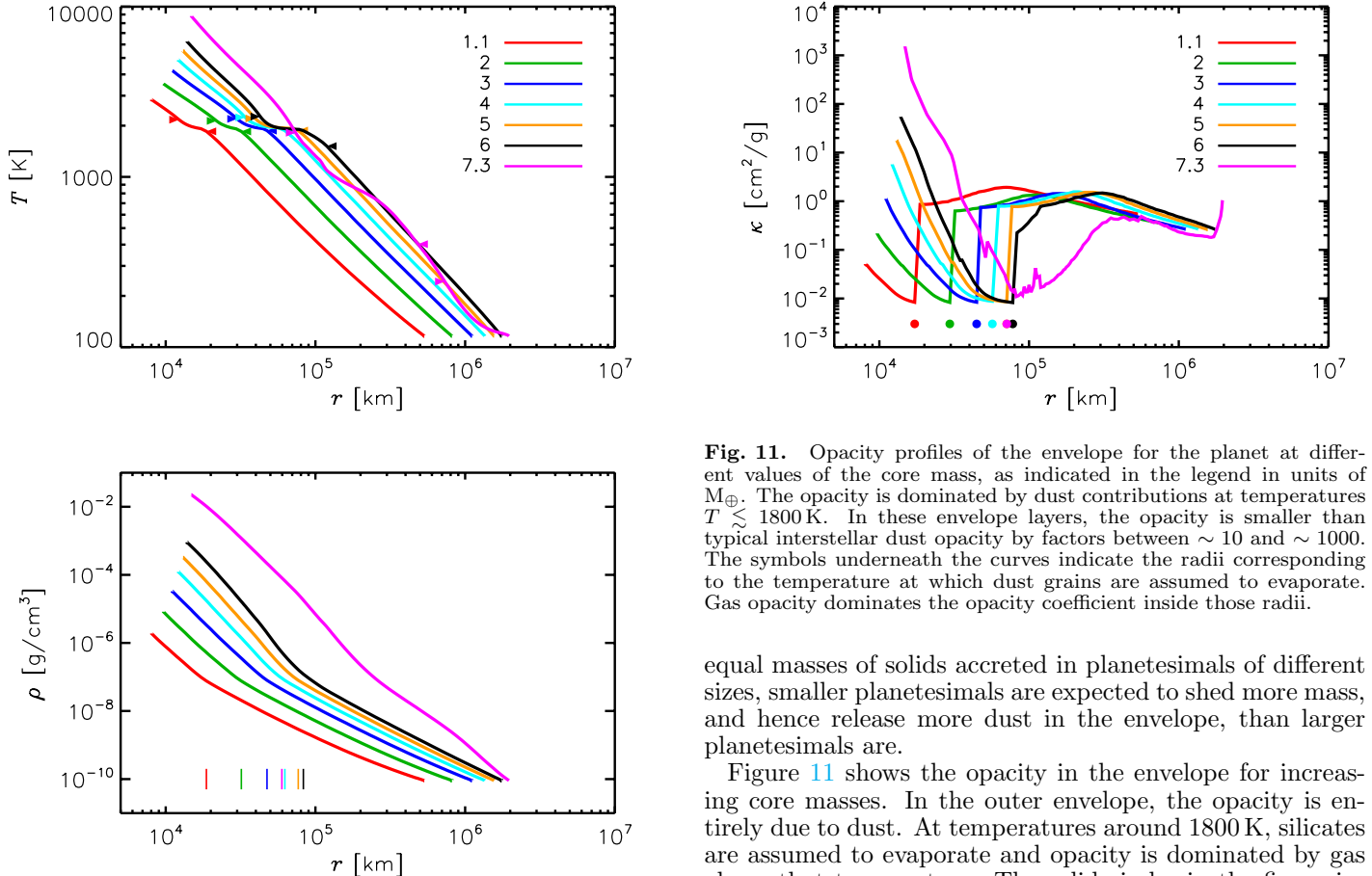


Fig. 10. Temperature (top panel) and density (bottom panel) profiles of the planet's envelope for various values of the core mass, as indicated in the legend of the top panel in units of M_\oplus . The temperature decrease in the outer layers between the envelope models at $M_c = 6$ and $7.3 M_\oplus$ is associated with the decrease in the core accretion rate (see top panel of Figure 8). The arrowheads (top) and the vertical line marks (bottom) indicate, respectively, the boundaries between convective and radiative layers and the radii where molecular hydrogen begins to dissociate.

Fig. 11. Opacity profiles of the envelope for the planet at different values of the core mass, as indicated in the legend in units of M_\oplus . The opacity is dominated by dust contributions at temperatures $T \lesssim 1800$ K. In these envelope layers, the opacity is smaller than typical interstellar dust opacity by factors between ~ 10 and ~ 1000 . The symbols underneath the curves indicate the radii corresponding to the temperature at which dust grains are assumed to evaporate. Gas opacity dominates the opacity coefficient inside those radii.

equal masses of solids accreted in planetesimals of different sizes, smaller planetesimals are expected to shed more mass, and hence release more dust in the envelope, than larger planetesimals are.

Figure 11 shows the opacity in the envelope for increasing core masses. In the outer envelope, the opacity is entirely due to dust. At temperatures around 1800 K, silicates are assumed to evaporate and opacity is dominated by gas above that temperature. The solid circles in the figure indicate the approximate radii in the envelopes at which dust grains evaporate and molecules dominate the opacity coefficient ([Freedman et al. 2008](#)). The accretion of gas is dictated by the contraction of the envelope, which is regulated by the ability of the outer layers to radiate energy away, which in turn depends on the opacity of these layers. The figure indicates that κ is between ~ 0.01 and $\sim 1 \text{ cm}^2 \text{ g}^{-1}$, one to three orders of magnitude smaller than the typical interstellar dust opacity. The minimum dust opacities are

higher than those in the models of MBPL10. The procedures for the opacity calculation are the same, but in the current study we include much smaller planetesimals. The difference may be caused in part by ablation of small planetesimals, although the envelope structure and solids accretion rates are different and therefore other effects may be important as well.

The opacity of the outer envelope layers is determined by the accretion rate of the gas, rather than by that of the solids. If the accretion flow delivers small grains to these layers on a timescale shorter than that required by the grains to coagulate and settle, the opacity is affected. Therefore, as \dot{M}_e begins to rise significantly, a gradual increase of κ should be expected at the outer boundary over time. Indeed, for $M_c > 6M_\oplus$, we observe that the opacity of the outermost layers steadily increases, with some fluctuations corresponding with variations of the gas accretion rate.

The top panel of Figure 8 shows that gas accretion starts to increase substantially only after solids accretion drops well below its maximum value. However, as argued above, the opacity is not only affected by the input rate of solids, \dot{M}_c , but also by the size of the bodies carrying the accreted mass. The accretion rates peak at planetesimals' radii between 30 and 50 kilometers. If the peak moved to smaller radii, a larger quantity of dust would be released in the outer envelope layers, increasing the opacity, delaying contraction, and reducing or possibly inhibiting the accretion of gas.

5. Summary and conclusions

We have modeled the growth of Jupiter's core at 5.2 AU from the proto-sun within a solar composition disk having a planetesimal surface mass density $\sigma_Z = 10(5.2 \text{ AU}/a) \text{ g cm}^{-2}$, where a is the heliocentric distance. Our simulations follow the evolution of solid bodies (see Figures 1 and 2) using the multi-zone accretion code developed by Weidenschilling et al. (1997) and Weidenschilling (2011), and modified as described in Section 2.1. This code accounts for gravitational interactions and gas drag, and assumes that physical collisions between solid bodies lead to accretion, or with sufficiently high impact velocities, to fragmentation. The planetary embryo begins as a Ceres-mass solid body (see Figure 9), but once it grows to a mass of $1.1M_\oplus$ it begins to accumulate a gaseous envelope whose quasi-hydrostatic structure and accretion of gas are calculated by means of the formalism described in Sections 2.5 through 2.8.

Relatively small fractions of the total mass of planetesimals are contained in bodies smaller than 1 km or larger than 100 km in radius. In fact, typically $< 9\%$ of the mass of the swarm is in planetesimals smaller than 1 kilometer in radius, $\lesssim 25\%$ is in planetesimals with radii between 1 and 10 kilometers, and $\lesssim 7\%$ is accounted for by bodies with radii larger than 100 kilometers. As the swarm evolves, mass is preferentially transferred to larger bodies. In particular, at the time when $M_c \approx 7M_\oplus$, about 80% of the mass is in the form of planetesimals with radii $10 \lesssim R \lesssim 130 \text{ km}$, and about 60% is accounted for by planetesimals whose radii are between ~ 20 and $\sim 80 \text{ km}$ (see Figure 3).

The core's growth rate initially accelerates rapidly via runaway accretion, but it eventually declines as accretion and shepherding combine to substantially depress the surface density of planetesimals in orbits surrounding the planet (see Figure 1). The core growth rate peaks at $2.2 \times$

$10^{-4} M_\oplus \text{ yr}^{-1}$ when $M_c \approx 2.1 M_\oplus$ (see Figure 8). Although the mass of the envelope remains small ($M_e \lesssim 10^{-3} M_\oplus$) until that of the core exceeds about $5 M_\oplus$, the envelope is large in volume, and is sufficiently dense to substantially increase the accretion rate of the core (by increasing the planet's capture cross-section for small planetesimals) once the planet's mass reaches $2 M_\oplus$ (see Figures 6 and 7). The gas accretion rate gradually increases, and becomes equal to the accretion rate of solids after about 4×10^5 years. At this time, the planet's core mass is $M_c \approx 7.3 M_\oplus$ and its envelope mass is $M_e \approx 0.15 M_\oplus$ (see Figures 8 and 9). A planet lacking an envelope would only grow to $4.4 M_\oplus$ at this time in the same disk (see Figure 4), and its growth rate at this point would be very small, $\dot{M}_c \approx 3 \times 10^{-7} M_\oplus \text{ yr}^{-1}$ (see Figure 8), as a consequence of gap clearing in the planetesimals' disk. In this case, because the shepherding effect depends on dissipation by collisions (mostly) and gas drag, we find that the mass limit is around 40% of the standard isolation mass (see Equation (3)).

We compare the results with previous models, which rely on estimates of solids accretion rates based on the three-body problem accretion calculations and planetesimals of a single size, and show that there are substantial differences (see Figure 8). One such calculation (Movshovitz et al. 2010), with the same σ_Z and the same envelope physics as the present simulation, gives the result, at the end of Phase 1 ($t \approx 0.45 \text{ Myr}$), of $M_c = 11.5 M_\oplus$ and $M_e = 0.67 M_\oplus$.

For a single size distribution of planetesimals with radius R , the mass ablated in an envelope layer is a fraction of the accreted mass (passing through that layer) proportional to $1/R$ (see discussion in Section 4). Therefore, smaller accreted bodies shed larger amounts of dust, possibly raising the envelope opacity (Movshovitz and Podolak 2008) and slowing envelope contraction. The fact that most of the accreted solid mass is in the form of relatively large planetesimals may favor the early growth of the gaseous envelope. Our results demonstrate the influence of a low-mass but voluminous planetary envelope on planetesimal accretion, and imply that Jupiter's core could have accumulated at the planet's current location in a protoplanetary disk whose surface mass density is only a few times as large as that of a classical minimum mass solar nebula.

Although the present study takes into account many physical processes relevant to the formation of a giant planet's core in a solar-type nebula, a number of effects are neglected. Among these are gas- and planetesimal-driven migration, trapping of bodies into mean motion resonances with the core, and the growth from the swarm of competing embryos. Inside $\sim 5 \text{ AU}$, gas-driven migration is thought to push inward cores less massive than about $10 M_\oplus$ (Baruteau et al. 2013) at a rate that appears very sensitive to the local (and time-varying) thermodynamical properties of the nebula gas. Planetesimal-driven migration in a disk of solids whose dynamics is dominated by Keplerian shear can potentially operate inward as well as outward (e.g., Kirsh et al. 2009; Levison et al. 2010; Capobianco et al. 2011, and references therein), depending on the details of both the planetesimal and the gas disks. Capture of bodies into mean motion resonances with the core may push it toward the sun (e.g., Levison et al. 2010), if the core is allowed to migrate. However, as the number density of bodies in and around the resonance region increases, collisions between planetesimals can become effective at altering their residence time in the resonance (Weidenschilling and Davis 1985). As al-

ready mentioned in Section 2.2, our calculations do allow for the possibility of oligarchic growth of multiple cores in the swarm of planetesimals and had we not started with a Ceres-sized seed body, multiple cores might have emerged. However, the seed body (which is only a factor of several larger than the largest bodies in the initial swarm) grows rapidly enough to inhibit potential competitors due to its perturbations. Clearly, a comprehensive calculation should attempt to include all of these (and other) effects, along with those included in this study.

References

- Adachi, I., Hayashi, C., Nakazawa, K., 1976. The gas drag effect on the elliptical motion of a solid body in the primordial solar nebula. *Progress of Theoretical Physics* 56, 1756–1771. [3](#)
- Alibert, Y., Mordasini, C., Benz, W., Winisdoerffer, C., 2005. Models of giant planet formation with migration and disc evolution. *Astron. Astrophys.* 434, 343–353. [2](#)
- Baruteau, C., Crida, A., Paardekooper, S.-J., Masset, F., Guilet, J., Bitsch, B., Nelson, R. P., Kley, W., Papaloizou, J. C. B., 2013. Planet-disc interactions and early evolution of planetary systems. Eprint arXiv:1312.4293. Protostars and Planets VI, edited by Beuther, H., Klessen, R., Dullemond, C. and Henning, T. Tucson, AZ: University of Arizona Press, in press. [15](#)
- Benvenuto, O. G., Fortier, A., Brunini, A., 2009. Forming Jupiter, Saturn, Uranus and Neptune in few million years by core accretion. *Icarus* 204, 752–755. [10](#)
- Bodenheimer, P., D'Angelo, G., Lissauer, J. J., Fortney, J. J., Saumon, D., 2013. Deuterium burning in massive giant planets and low-mass brown dwarfs formed by core-nucleated accretion. *Astrophys. J.* 770, 120. [2](#)
- Bodenheimer, P., Hubickyj, O., Lissauer, J. J., 2000. Models of the in situ formation of detected extrasolar giant planets. *Icarus* 143, 2–14. [7](#)
- Bodenheimer, P., Pollack, J. B., 1986. Calculations of the accretion and evolution of giant planets: the effects of solid cores. *Icarus* 67, 391–408. [1](#)
- Capobianco, C. C., Duncan, M., Levison, H. F., 2011. Planetesimal-driven planet migration in the presence of a gas disk. *Icarus* 211, 819–831. [15](#)
- Chambers, J. E., 2014. Giant planet formation with pebble accretion. *Icarus* 233, 83–100. [10](#), [11](#)
- Chiang, E., Youdin, A. N., 2010. Forming planetesimals in solar and extrasolar nebulae. *Annual Review of Earth and Planetary Sciences* 38, 493–522. [1](#)
- D'Angelo, G., Durisen, R. H., Lissauer, J. J., 2011. Giant Planet Formation. *Exoplanets*, edited by S. Seager. Tucson, AZ: University of Arizona Press, pp. 319–346. [4](#)
- Davis, D. R., Ryan, E. V., Farinella, P., 1994. Asteroid collisional evolution: Results from current scaling algorithms. *Planet. Space Sci.* 42, 599–610. [4](#)
- Dodson-Robinson, S. E., Bodenheimer, P., Laughlin, G., Willacy, K., Turner, N. J., Beichman, C. A., 2008. Saturn forms by core accretion in 3.4 Myr. *Astrophys. J.* 688, L99–L102. [4](#)
- Fortney, J. J., Nettelmann, N., 2010. The interior structure, composition, and evolution of giant planets. *Space Sci. Rev.* 152, 423–447. [2](#)
- Fortier, A., Benvenuto, O. G., Brunini, A., 2007. Oligarchic planetesimal accretion and giant planet formation. *Astron. Astrophys.* 473, 311–322. [10](#)
- Fortier, A., Benvenuto, O. G., Brunini, A., 2009. Oligarchic planetesimal accretion and giant planet formation II. *Astron. Astrophys.* 500, 1249–1252. [10](#)
- Freedman, R. S., Marley, M. S., Lodders, K., 2008. Line and mean opacities for ultracool dwarfs and extrasolar planets. *Astrophys. J.* S. 174, 504–513. [14](#)
- Greenberg, R., 1983. The role of dissipation in shepherding of ring particles. *Icarus* 53, 207–218. [4](#)
- Greenberg, R., Bottke, W. F., Carusi, A., Valsecchi, G. B., 1991. Planetary accretion rates - Analytical derivation. *Icarus* 94, 98–111. [3](#)
- Greenzweig, Y., Lissauer, J. J., 1990. Accretion rates of protoplanets. *Icarus* 87, 40–77. [3](#), [5](#)
- Greenzweig, Y., Lissauer, J. J., 1992. Accretion rates of protoplanets. II - Gaussian distributions of planetesimal velocities. *Icarus* 100, 440–463. [3](#), [5](#), [11](#), [14](#)
- Guilera, O. M., Fortier, A., Brunini, A., Benvenuto, O. G., 2011. Simultaneous formation of solar system giant planets. *Astron. Astrophys.* 532. Article ID: A142. [10](#)
- Hairer, E., Nørsett, S. P., Wanner, G., 1993. Solving Ordinary Differential Equations I: Nonstiff Problems. Springer Series in Computational Mathematics, Vol. 8, 2nd ed. Springer-Verlag Berlin Heidelberg. [9](#)
- Hayashi, C., 1981. Structure of the solar nebula, growth and decay of magnetic fields and effects of magnetic and turbulent viscosities on the nebula. *Progress of Theoretical Physics Supplement* 70, 35–53. [1](#)
- Hillenbrand, L. A., 2008. Disk-dispersal and planet-formation timescales. *Physica Scripta Volume T* 130 (1), 014024. [2](#)
- Hubickyj, O., Bodenheimer, P., Lissauer, J. J., 2005. Accretion of the gaseous envelope of Jupiter around a 5–10 Earth-mass core. *Icarus* 179, 415–431. [7](#)
- Iaroslavitz, E., Podolak, M., 2007. Atmospheric mass deposition by captured planetesimals. *Icarus* 187, 600–610. [9](#)
- Inaba, S., Wetherill, G. W., Ikoma, M., 2003. Formation of gas giant planets: Core accretion models with fragmentation and planetary envelope. *Icarus* 166, 46–62. [2](#)
- Kary, D. M., Lissauer, J. J., 1994. Numerical simulations of planetary growth. *Numerical Simulations in Astrophysics*, edited by Franco, J., Lizano, S., Aguilar, L., and Daltabuit, E. Cambridge: Cambridge University Press, pp. 364–373. [4](#)
- Kary, D. M., Lissauer, J. J., 1995. Nebular gas drag and planetary accretion. II. Planet on an eccentric orbit. *Icarus* 117, 1–24. [3](#)
- Kary, D. M., Lissauer, J. J., Greenzweig, Y., 1993. Nebular gas drag and planetary accretion. *Icarus* 106, 288–307. [3](#)
- Kippenhahn, R., Weigert, A., Weiss, A., 2013. *Stellar Structure and Evolution*. Springer-Verlag Berlin Heidelberg. [7](#)
- Kirsh, D. R., Duncan, M., Brasser, R., Levison, H. F., 2009. Simulations of planet migration driven by planetesimal scattering. *Icarus* 199, 197–209. [15](#)
- Kobayashi, H., Tanaka, H., Krivov, A. V., 2011. Planetary core formation with collisional fragmentation and atmosphere to form giant planets. *Astrophys. J.* 738, 35. [10](#)
- Kobayashi, H., Tanaka, H., Krivov, A. V., Inaba, S., 2010. Planetary growth with collisional fragmentation and gas drag. *Icarus* 209, 836–847. [10](#)
- Lambrechts, M., Johansen, A., 2012. Rapid growth of gas-giant cores by pebble accretion. *Astron. Astrophys.* 544. Article ID: A32. [10](#)
- Levison, H. F., Thommes, E., Duncan, M. J., 2010. Modeling the formation of giant planet cores. I. Evaluating key processes. *Astron. J.* 139, 1297–1314. [10](#), [15](#)
- Lissauer, J. J., 1987. Timescales for planetary accretion and the structure of the protoplanetary disk. *Icarus* 69, 249–265. [4](#)
- Lissauer, J. J., Hubickyj, O., D'Angelo, G., Bodenheimer, P., 2009. Models of Jupiter's growth incorporating thermal and hydrodynamic constraints. *Icarus* 199, 338–350. [2](#), [8](#)
- Lissauer, J. J., Stewart, G. R., 1993. Growth of planets from planetesimals. *Protostars and Planets III*, edited by Levy, E. H. and Lunine, J. I. Tucson, AZ: University of Arizona Press, pp. 1061–1088. [4](#)

Acknowledgments

This project was funded by NASA Outer Planets Research Program Grant 202844.02.02.01.75. We are grateful to Olenka Hubickyj for helpful discussions and useful feedback on this work, and to two anonymous referees whose comments and suggestions helped improve this paper. G.D. thanks Los Alamos National Laboratory for its hospitality. Resources supporting this study were provided by the NASA High-End Computing (HEC) Program through the NASA Advanced Supercomputing (NAS) Division at Ames Research Center and the NASA Center for Climate Simulation (NCCS) at Goddard Space Flight Center.

- Lubow, S. H., Ida, S., 2011. Planet Migration. *Exoplanets*, edited by S. Seager. Tucson, AZ: University of Arizona Press, pp. 347–371. [4](#)
- Militzer, B., Hubbard, W. B., Vorberger, J., Tamblyn, I., Bonev, S. A., 2008. A massive core in Jupiter predicted from first-principles simulations. *Astrophys. J.* 688, L45–L48. [2](#)
- Mizuno, H., 1980. Formation of the giant planets. *Progress of Theoretical Physics* 64, 544–557. [1](#)
- Morbidelli, A., Nesvorný, D., 2012. Dynamics of pebbles in the vicinity of a growing planetary embryo: Hydro-dynamical simulations. *Astron. Astrophys.* 546. Article ID: A18. [10](#)
- Mordasini, C., Alibert, Y., Georgy, C., Dittkrist, K.-M., Klahr, H., Henning, T., 2012. Characterization of exoplanets from their formation. II. The planetary mass-radius relationship. *Astron. Astrophys.* 547, A112. [2](#)
- Movshovitz, N., Bodenheimer, P., Podolak, M., Lissauer, J. J., 2010. Formation of Jupiter using opacities based on detailed grain physics. *Icarus* 209, 616–624. [2](#), [4](#), [8](#), [11](#), [12](#), [13](#), [14](#), [15](#)
- Movshovitz, N., Podolak, M., 2008. The opacity of grains in protoplanetary atmospheres. *Icarus* 194, 368–378. [15](#)
- Nettelmann, N., Becker, A., Holst, B., Redmer, R., 2012. Jupiter models with improved ab initio hydrogen equation of state (H-REOS.2). *Astrophys. J.* 750, 52. [2](#)
- Nishida, S., 1983. Collisional processes of planetesimals with a protoplanet under the gravity of the proto-Sun. *Progress of Theoretical Physics* 70, 93–105. [3](#), [4](#)
- Ormel, C. W., Klahr, H. H., 2010. The effect of gas drag on the growth of protoplanets. Analytical expressions for the accretion of small bodies in laminar disks. *Astron. Astrophys.* 520. Article ID: A43. [10](#)
- Owen, T., Mahaffy, P., Niemann, H. B., Atreya, S., Donahue, T., Bar-Nun, A., de Pater, I., 1999. A low-temperature origin for the planetesimals that formed Jupiter. *Nature* 402, 269–270. [2](#)
- Perri, F., Cameron, A. G. W., 1974. Hydrodynamic instability of the solar nebula in the presence of a planetary core. *Icarus* 22, 416–425. [1](#)
- Podolak, M., Pollack, J. B., Reynolds, R. T., 1988. Interactions of planetesimals with protoplanetary atmospheres. *Icarus* 73, 163–179. [8](#), [13](#)
- Pollack, J. B., Hubickyj, O., Bodenheimer, P., Lissauer, J. J., Podolak, M., Greenzweig, Y., 1996. Formation of the giant planets by concurrent accretion of solids and gas. *Icarus* 124, 62–85. [1](#), [2](#), [4](#), [5](#), [7](#)
- Roberge, A., Kamp, I., 2011. Protoplanetary and Debris Disks. *Exoplanets*, edited by S. Seager. Tucson, AZ: University of Arizona Press, pp. 269–295. [2](#)
- Safronov, V. S., 1972. Evolution of the protoplanetary cloud and formation of the Earth and planets. Evolution of the protoplanetary cloud and formation of the Earth and planets. Edited by Safronov, V. S.. Translated from Russian. Israel Program for Scientific Translations. Keter Publishing House, Jerusalem, Israel. [1](#)
- Saumon, D., Guillot, T., 2004. Shock compression of deuterium and the interiors of Jupiter and Saturn. *Astrophys. J.* 609, 1170–1180. [2](#)
- Tanaka, H., Ida, S., 1997. Distribution of planetesimals around a protoplanet in the nebula gas. *Icarus* 125, 302–316. [4](#)
- Weidenschilling, S. J., 1977. The distribution of mass in the planetary system and solar nebula. *Astrophysics and Space Science* 51, 153–158. [1](#)
- Weidenschilling, S. J., 1989. Stirring of a planetesimal swarm - The role of distant encounters. *Icarus* 80, 179–188. [3](#)
- Weidenschilling, S. J., 2005. Formation of the cores of the outer planets. *Space Science Reviews* 116, 53–66. [2](#), [4](#)
- Weidenschilling, S. J., 2011. Initial sizes of planetesimals and accretion of the asteroids. *Icarus* 214, 671–684. [3](#), [15](#)
- Weidenschilling, S. J., Davis, D.R., 1985. Orbital resonances in the solar nebula - Implications for planetary accretion. *Icarus* 62, 16–29. [15](#)
- Weidenschilling, S. J., Spaute, D., Davis, D. R., Marzari, F., Ohtsuki, K., 1997. Accretional evolution of a planetesimal swarm. *Icarus* 128, 429–455. [3](#), [15](#)
- Wetherill, G. W., Stewart, G. R., 1989. Accumulation of a swarm of small Planetesimals. *Icarus* 77, 330–357. [3](#)
- Young, R. E., 2003. The Galileo probe: How has it changed our understanding of Jupiter? *New Astronomy Reviews* 47, 1–51. [2](#)
- Young, R. E., Smith, M. A., Sobeck, C. K., 1996. Galileo probe: In situ observations of Jupiter's atmosphere. *Science* 272, 837–838. [2](#)